LASER DESORPTION MASS SPECTROMETRY AND SMALL ANGLE NEUTRON SCATTERING OF HEAVY FOSSIL MATERIALS

Jerry E. Hunt[1], Randall E. Winans[1], and P. Thiyagarajan[2]
[1]Chemistry Division
[2]Intense Pulsed Neutron Division
Argonne National Laboratory
9700 South Cass Ave.
Argonne, IL 60439

INTRODUCTION

The determination of the structural building blocks and the molecular weight range of heavy hydrocarbon materials is of crucial importance in research on their reactivity and for their processing. The chemically and physically heterogenous nature of heavy hydrocarbon materials, such as coals, heavy petroleum fractions, and residues, dictates that their structure and reactivity patterns be complicated. The problem is further complicated by the fact that the molecular structure and molecular weight distribution of these materials is not dependent on a single molecule, but on a complex mixture of molecules which vary among coals and heavy petroleum samples. Laser Desorption mass spectrometry (LDMS) is emerging as a technique for molecular weight determination having found widespread use in biological polymer research, but is still a relatively new technique in the fossil fuel area. Small angle neutron scattering (SANS) provides information on the size and shape of heavy fossil materials. SANS offers the advantages of high penetration power even in thick cells at high temperatures and high contrast for hydrocarbon systems dispersed in deuterated solvents. LDMS coupled with time of flight has the advantages of high sensitivity and transmission and high mass range. We have used LDMS to examine various heavy fossil-derived materials including: long chain hydrocarbons, asphaltenes from petroleum vacuum resids, and coals. This paper describes the application of laser desorption and small angle neutron scattering techniques to the analysis of components in coals, petroleum resids and unsaturated polymers.

EXPERIMENTAL

The coals used in this study are the Argonne Premium Coal Samples. The procedures for the pyridine extract of the Argonne Premium Coals have been reported previously. The laser desorption mass spectra were recorded on a linear time-of-flight mass spectrometer constructed at Argonne and a Kratos Kompact MALDI III linear/reflectron time-of-flight mass spectrometer. The spectra were produced by exposing the samples distributed as thin layer on a stainless steel sample holder to laser pulses a nitrogen laser. The laser is operated close to the ionization threshold to minimize possible fragmentation of the desorbing material and to optimize resolution. The polyethylene sample were purchased from Petrolite.

Pentane soluble, heptane precipitated asphaltenes and the deasphalted oil (DAO) from vacuum resids of Maya crude oil were obtained from Amoco. The d10-1-methylnaphthalene (d_{10}-1MN) was obtained from Aldrich. Five wt.% dry asphaltene was dissolved in d_{10}-1MN and the solution was stirred overnight. Small angle neutron scattering was performed by placing the sample cell in a boron nitride furnace tube in the small angle diffractometer (SAD) at the Intense Pulsed Neutron Source (IPNS) at Argonne National Laboratory. The temperature of the furnace was measured using a type K thermocouple and maintained within 0.5°C using a Micricon controller. The SAD instrument uses neutrons produced in pulses by spallation due to the deposition of 450 MeV protons on a depleted uranium target, followed by a solid methane moderator (22 K) yielding a wavelength range of 1 to 14Å. Detection of scattered neutrons was accomplished with a 128 x 128 array, 40X40 cm^2 area sensitive, gas-filled proportional counter, and the wavelength of the scattered neutrons was determined by their times-of-flight. Data were corrected for unit transmission of the sample, the scattering from the stainless steel cell, and incoherent scattering. The accessible q range ($q= 4\pi\sin(q)/l$ where l is the wavelength of the probing neutrons and q is half the scattering angle) using SAD is from 0.008 to 0.2 $Å^{-1}$.

RESULTS AND DISCUSSION

The mechanisms at work in laser desorption of ions from surfaces is a subject of much speculation and conjecture. Despite the complexity of the ionization mechanism, the facts remain that mass spectra of a large number of volatile organic compounds can be generated by laser desorption at threshold powers and that fragmentation of the parent molecule is minimal at best. Higher laser fluences may alter the ionization process to result in destructive fragmentation, in structurally significant fragmentation, or even ion-molecule reactions. In addition, the desorption event may cause 'clustering' of molecules leading to mis-interpretations of the data, i.e., incorrectly assuming that larger molecules are present.

Figure 1 presents the laser desorption mass spectrum of a polyethylene sample of 1000 molecular weight. A silver nitrate matrix is used to produce LD mass spectra of polyethylene by cationization. Each ion is an adduct of silver.

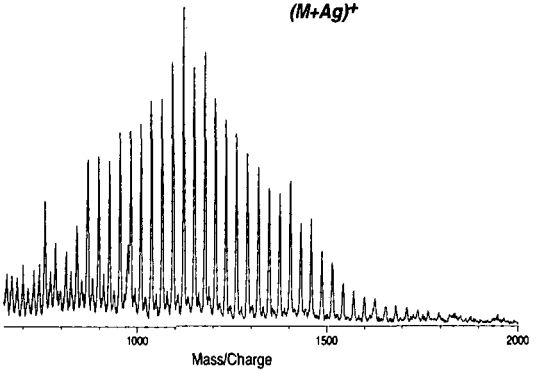

Figure 1. The LDMS spectrum of polyethylene 1000. The ions are produced by cationization with Ag.

Polymer statistics can be calculated from the data. The repeat unit of the polymer can be directly calculated from the mass difference of the oligomer units, and the end groups can also be ascertained. The integrated peak areas (N_i) are used with oligomer molecular weights (M_i) to calculate the number average (M_n) and weight average (M_w) as follows:

$$M_n = N_iM_i / N_i$$
$$M_w = N_iMi^{2}/N_i$$
$$\text{polydispersity} = M_w/M_n$$

For the polyethylene polymer the number average is 1006 and the weight average is 1045 with a polydispersity of 1.04. To be sure there are some difficulties in these analyses. The lack of polar sites on this compound makes ionization difficult, as ionization in LD generally depends on either low ionization potential with adsorption of the compound (an example is aromatic compounds) or availability of a polar group to which either proton attachment or cationization can occur. One of the practical difficulties of integrating spectra of polymer distribution is knowing where to draw a representative baseline. Very polydisperse systems tend to be problematic.

Coal extracts are readily amenable to LD. Figure 2 shows the LDMS spectra of a homologous ion series found in the pyridine extract of Wyodak coal (APCS 2). One of the strengths of direct LD is that aromatic components are easily ionized and detected.

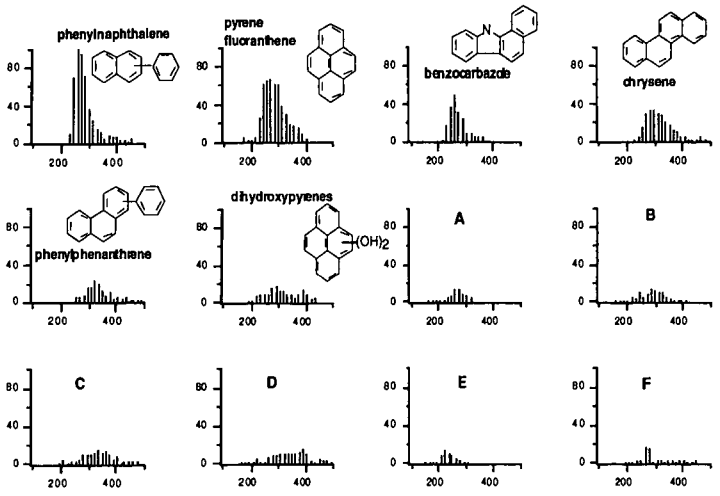

Figure 2. LDMS spectra of the homologous ion series in the pyridine extract of Wyodak-Anderson subbituminous coal (APCS 2)

An interesting result is the four ring systems found in the subbituminous coal. Other ion series, at lower intensities, that have yet to be completely identified (labeled as A, B, C, etc.) show strong evidence for five and six ring systems.

As LDMS is known to chiefly access the aromatic content of a sample, the LDMS of Maya petroleum resid asphaltenes show intense mass spectra like the coal extracts because of their strong aromatic content. The asphaltenes, however, show a higher average molecular weight and a broader molecular weight distribution. The asphaltene has ion intensity extending form a m/z range of ca. 200 to ca. 750. The mass distribution tails to 1000 with exponentially decreasing intensity. Very large molecular species (>1500) are not observed in the asphaltene. The number average molecular weight is quite low, on the order of 500, while the weight average molecular weight, which is more sensitive to the extent of the mass distribution, is on the order of 750. The sample can be considered as a very polydisperse system, at least to first order. Thus, drawing a base line for the high mass region is difficult at best so an upper bound on mass is not possible. However, the bulk of sample has a fairly low molecular weight (about 500 amu).

Gel permeation chromatography and vapor phase osmometry experiments on the asphaltenes indicate that they are rather large structures. GPC shows two size distributions for asphaltenes at approximately 225 and 80 Å. Such structures should have molecular weight very much higher than those found by mass spectrometry. We have, thus, turned to small angle neutron scattering (SANS) to determined the size and shapes of the asphaltenes in solution. SANS was used to investigate the structural changes of a 5 wt.% asphaltene solution in perdeuterated 1-methylnaphthalene (d-1MN) as a function of temperature. A special stainless steel cell was constructed and used for the measurements. The SANS data measured at various temperatures from 20°C to 400°C show that the scattering intensity continuously decreases with increasing temperature. A nonlinear curve in the Guinier plot for asphaltene solutions at 20°C suggested polydispersity in the sizes. Maximum entropy analysis using the form factor for a cylinder allowed extraction of particle size distributions in the radius and length space.

At 20°C the asphaltenes self-associate in d-1MN forming long rod-shaped particles whose radius was around 18Å, but vary in length over 500Å. At 50°C these aggregates break down, as evidenced by the decrease in signal intensity.

In the temperature range of 100 - 320°C the maximum length of the particles decreases and the polydispersity varies in both radius and length dimensions. Between 340 and 400°C, the particles become smaller having a spherical shape with a radius around 12Å.

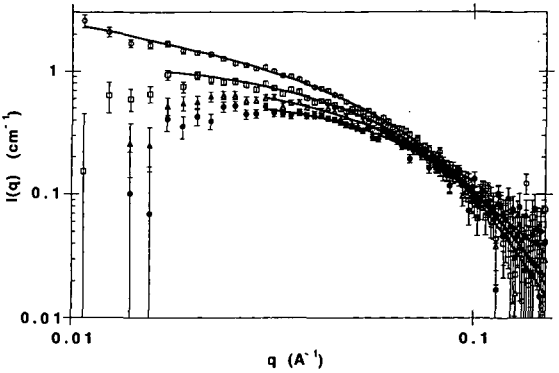

Figure 3: Maximum entropy fits of the SANS data for 5 wt.% asphaltenes in d-1MN at 20°C (o), 50°C (square), 150°C (triangle) and 400°C (filled o).

Upon returning the sample to 20°C, the SANS signal was too weak to derive any structural information, implying irreversible thermochemistry. Interestingly, the structural properties of asphaltenes in d-1MN at temperatures below irreversibility are remarkably reproducible, irrespective of the temperature sequence steps.

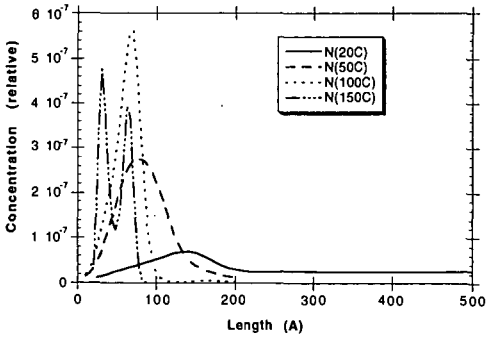

Figure 4: The length distributions for the asphaltene solutions in d-1MN: 20°C (solid line), 50°C(dashed line), 100°C (dotted line), 150°C (dashed-dotted line). The radius is approximately 20 Å for all samples.

Figure 3 shows that maximum entropy analysis is very effective in obtaining the morphology and polydispersity information of the asphaltenes. Figure 4 shows the length distribution for particles of a given radius at 4 different temperatures. The mass spectrometric data and SANS data show that asphaltenes are indeed composed of chiefly low molecular weight molecules (perhaps as low as 500 amu) and that at ambient temperatures aggregate strongly.

Acknowledgment. This work was supported by the Division of Chemical Sciences, Office of Basic Energy Sciences, U. S. Department of Energy, under contract W-31-109-ENG-38.

ANOMALOUS SMALL ANGLE X-RAY SCATTERING STUDIES OF HEAVY METAL ION SOLVATION BEHAVIOR IN CLAY MINERALS

Kathleen A. Carrado*, Kang Song, Randall E. Winans, and P. Thiyagarajan†
Chemistry Division and †Intense Pulsed Neutron Source Division
Argonne National Laboratory, 9700 S. Cass Ave., Argonne, IL 60439

ABSTRACT

We have exploited anomalous small angle x-ray scattering (ASAXS) to monitor the solvation behavior of Cu(II), Er(III) and Yb(III) ions within the interlayers of the natural aluminosilicate clay mineral montmorillonite. The ASAXS technique can reveal the distribution of specific metallic species within a heterogeneous and disordered matrix. The variations of signal intensity as a function of absorption energy were monitored for all of the metal-clays as a function of hydration. Two different hydration levels were probed: as prepared at ambient conditions, or so-called "dry" powders, and "wet" pastes. ASAXS intensities should increase as the energy of the probing x-rays approaches the absorption energy of a given metal ion if it is associated with the interlayer solvent (water in this case), and decrease if the metal ion is associated with the solid matrix. The results show that: (1) Cu(II) is solvated within the interlayers of the wet sample, as expected, and (2) Er(III) and Yb(III) decrease in ASAXS intensity with increased hydration. This latter result was not expected and there is speculation that these ions have associated as hydrolyzed products with the clay surface. The basic principles underlying SAXS and ASAXS will also be presented in this paper.

INTRODUCTION

Clay Minerals

Our interest in clays in terms of fuels science applications has two origins: (1) they are an inherent constituent in the mineral matter of coal and (2) their use as catalysts or catalyst supports in such processes as heavy petroleum upgrading. Small amounts of metal loadings on clays has relevance to both of these facets. Smectite clay minerals are layered metal silicates whose sheets can swell to incorporate up to several layers of water molecules. Each sheet is made up of one octahedral metal oxide layer, usually aluminum or magnesium, that is sandwiched by two tetrahedral silicate layers. Isomorphous substitutions within this framework give rise to a net negative charge on the lattice that is compensated for by the presence of exchangeable ions within the hydrated interlayer. Clays have a long history of applications as catalysts, catalyst supports, adsorbents, and ion-exchangers[1]. They are also prevalent in the mineral matter of coal, effecting it's combustion, processing, and conversion properties[2].

Clay minerals can incorporate heavy metal ions both within the lattice framework and between the interlayer regions. Our ASAXS investigation into the former situation has been published elsewhere[3]. For the latter case, clays ion-exchanged with various transition metal and lanthanide ions (Fig. 1), have been examined in hydrated and non-hydrated forms. The exchangeable interlayer metal ions impart a surface acidity on the clay that is variable depending upon the type of metal cation and the amount of water present within the interlayer[1]. This surface acidity is vital to many hydro-processing reactions of importance to petroleum refining, for example. In addition to catalytic applications, these experiments are also pertinent to the structure, diffusion, and reactivity of species involved in, for example, environmental remediation issues. A preliminary report of Er(III)-clay ASAXS[3] has now been expanded to include several different metal ions.

SAXS And ASAXS Methodology

A description of both local and long-range atomic order associated with molecular assemblies in disordered media is essential for understanding the molecular basis for such issues as catalysis. Examples of such order include the structure and dynamics of molecular catalysts in solution, and the distribution of solvent, solute, and counterions around catalytic surface sites. X-ray scattering provides a powerful tool for the measurement of long-range atomic order in globally disordered media. Disordered systems far more frequently describe materials used in the "real" world, yet they do not lend themselves to characterization by many of the standard techniques appropriate

only for well-defined, ordered materials. In addition to this, the use of ASAXS to probe atomic order in condensed media is in its infancy because it has been limited by the inherent weakness of the signals. Our initial studies[3] represent the first preliminary steps into this arena.

Small angle X-ray scattering (SAXS) has numerous applications in chemistry, metallurgy, biology, polymer science, and colloidal systems. It examines correlations at distances from 10 Å to 1000 Å and provides information about the size, morphology, and interactions of a system of particles or pores in solution or the solid state. SAXS can also be used to follow the phase transitions, crystallization, and aggregation within a system. The SAXS intensity as a function of the momentum transfer is due to the distance correlations of all the atoms in the particles of interest. Anomalous small angle X-ray scattering (ASAXS) refers to extensions of standard SAXS experiments in which the energy of the probing X-rays are tuned near the absorption edge of an element in the sample. By performing SAXS experiments near the characteristic absorption edge of any given atom, it is possible to vary the contrast for scattering of that particular element. This systematic variation in contrast yields the partial scattering functions of the specific atomic species. In general, the atomic scattering can be expressed as:

$$f(q,E) = f_o(q) + f'(q,E) + if''(q,E) \qquad (1)$$

where E is the energy of the probing X-rays and q is the momentum transfer ($q=4\pi\sin\theta/\lambda$, where 2θ is the scattering angle and λ is the wavelength of X-rays). The parameters f' and f'' are the real and imaginary parts of anomalous dispersion. They each vary sharply at energies within 10 eV of the absorption edge. The imaginary scattering factor, f'', represents the absorption of X-rays which results in photoemission of a core electron. Variation in f' is responsible for the change in contrast seen in ASAXS signals. These two quantities are related by the Kramers-Kronig relation. Typically f' is determined by measuring the energy-dependent absorption spectrum, f'', and applying the Kramers-Kronig transformation. Near the absorption edge of a given atom the scattering intensity, I, varies as a function of energy or wavelength (equation 2).

$$I(q,\lambda) = I_o(q) + f'(\lambda)I_C(q,\lambda) + [f'^2(\lambda) + f''^2(\lambda)]\, I_R(q) \qquad (2)$$

Here I_o represents the nonresonant, energy-independent scattering. The cross term, I_C, reflects scattering between the specific element of interest and the remainder of the material, while I_R corresponds to the distance correlations of just the resonant scatterers.

Since f' and f'' are sharply varying functions near the edge, these experiments require the highest possible energy resolution (of the order of $\Delta\lambda/\lambda=10^{-4}$) for the probing monochromatic X-rays. In these experiments we determine the small angle scattering using incoming X-rays with 4 to 5 different energies. All but one of these energies are near the absorption edge of the atom of interest. The last measurement, using X-rays whose energy is 150 eV below the edge, gives a direct measurement of the nonresonant scattering, I_o, since at this energy f' and f'' are effectively zero. From these sets of data, in principle one can obtain a set of 3 to 4 differential scattering data after the subtraction of I_o. If the SAXS data as a function of energy are placed on an absolute scale, one can then use f' and f'' values to obtain the partial structure factors, I_C and I_R, by least square analysis. The maximum variation in the SAXS signals near the edge depends on the maximum value of the variation of f' for a given atom. In general, the variation of f' is larger near the L_{III} edges than for the K edges. Therefore, if a transition metal ion is of interest, generally a larger weight % is necessary. This is true until higher power sources such as the Advanced Photon Source come on line in the very near future.

ASAXS is a very new technique, first reported in 1985 for the analysis of metal alloys[4a] (and somewhat earlier for biochemical systems[4b,c]). Some review articles are available with general background information for the interested reader[5,6]. Only a few references exist where ASAXS has been exploited to characterize heterogeneous catalysts or supports[3,7].

EXPERIMENTAL

Bentolite L, a natural Ca^{2+}-bentonite that has been purified to remove all but 0.2 wt% Fe impurities, was obtained from Southern Clay Products. This was ion-exchanged with Cu(II), Er(III), and Yb(III) ions by stirring 1 gm clay in 100 ml of 0.1M solutions of the hydrated chloride salts overnight, followed by centrifugation, washing, and drying at room temperature. X-ray powder diffraction patterns were obtained on a Scintag PAD V instrument with Cu K_α radiation.

The powder and thick slurry samples were contained in a cell with kapton windows for SAXS measurements. The samples were measured at SAXS beamline BL 4-2 at the Stanford Synchrotron Radiation Laboratory in Stanford, CA. This beamline has a platinum coated mirror which focuses the X-rays in the horizontal direction. A 62 μRad slit upstream from this mirror defines the energy resolution of the probing X-rays at <2 eV. The reflected beam from the mirror is monochromated by a double-crystal Si(111) monochromator. The cross-sectional area of the X-ray beam, 3 mm x 1 mm, is defined by two slits. The beam was focused at a 20 cm long 1-dimensional position sensitive gas detector. The sample was located approximately 2.2 m upstream to the detector. Two ionization chambers, one before and one after the sample, monitored the intensity of the incident and absorbed X-rays. These monitors were also used to determine the absorption edge for the metal of interest in each of the samples. The entire beam path was under vacuum except at the sample. In this configuration the SAXS instrument can measure data in the q region from 0.008 to 0.25 $Å^{-1}$.

The acquisition time for each scattering profile was 5 minutes. During the acquisition of the scattering data, the energy of the incoming X-rays was cycled through each of the energies for 5 to 10 cycles, depending on the desired statistical precision. This procedure aided in the assessment of the stability of the sample, as well as the position of the X-ray beam. For Er-clays, an absorption edge at 8372.6 eV corresponding to the L_{III} edge of Er(III) was found. The ASAXS for the powder samples were then measured at 8100, 8355, 8368, 8370 and 8372 eV. Similar procedures were used for the remaining metal ions using their respective absorption energy edges.

RESULTS AND DISCUSSION

The dry and wet samples were analyzed by ASAXS and x-ray powder diffraction (XRD). XRD revealed that the interlayer spacings for all metal-clays increased by 4-5 Å upon hydration (formation of a wet paste) to 19.5 - 20 Å. This indicates that the interlayer has accommodated more water layers. Typically, they expand from one or two layers of water to three layers[3]. Modified Guinier analysis of the ASAXS data was used to extract the correlations for these sheet-like particles. This approach is based on the fact that the intensity of scattering for infinitely large sheets varies as q^{-2}.[8] When a Guinier analysis is performed in the low-q region by plotting $\ln[q^2 \cdot I(q)]$ as a function of q^2, a linear region indicates the presence of sheet-like particles. Figures 1 and 2 display the modified Guinier sheet analyses for the Cu(II)-clay and Yb(III)-clay systems, respectively. Results for Er(III)-clay were similar to Yb(III)-clay.

ASAXS intensities should increase with absorption energy if the metal ion is associated with the interlayer solvent (water, in this case), and decrease if the metal ion is associated with the solid matrix[3]. The following discussion is provided to explain these various intensity changes. The scattering cross section of a given system is determined by the atomic scattering factor f' of the constituent atoms. The f' factor includes two terms: Z, which is the number of electrons in a given atom, and a dispersion term which strongly varies only near the edge. Near the characteristic absorption edge f' has a minimum.

Let us consider the system of dispersed clay particles in water. The scattering from this system is determined by the number density of the particles, square of the volume of the particles, and the square of the difference in the electron densities of the particles and water. Note that the electron density of clays will always be higher than that of water. In this scenario, if the labels of interest are located within the clay lattice itself (e.g. Ni-SMM clay[3]), the difference in the electron density between the clay and the water will decrease as one approaches the absorption edge of a given metal atom. This is because the net f' value will decrease while that of the H_2O remains the same. That means that the electron density difference decreases as the energy of the probing x-rays approaches the edge and thus the scattering intensity should monotonically decrease with increasing energy[6].

On the other hand, if the metal atoms are associated with the solvent but not with the clays, then f' of the clay remains the same, but that of the solvent decreases. This means that the net electron density difference increases as one approaches the absorption edge. This will result in a monotonic increase in the scattering intensity with increasing energy as the energy of the probing x-rays approaches the absorption edge of a given atom[6].

For the same concentration of the metal atoms, the above effect will be much larger for the former case (ion-clay interaction) than that for the latter (ion-solvent interaction). This is because the signal intensity that is due to constructive interference from the scattering waves from the labels in clays is completely lost from similar atoms in solution.

Although there is a very slight ASAXS effect observed in the "dry" samples (Figs. 1a and 2a), the margin of error precludes us from deducing where the ions might reside. Much more of an effect is observed for the wet samples. Based on the XRD results of increased basal spacings with addition of water, we were expecting in all cases to see that the ions would be associated with the solvent (water) in the slurries. This did occur for the Cu-clay, corroborating our results from a local-environment, short-range order study by x-ray absorption spectroscopy9. However, neither of the Ln-clays showed an ion-solvent interaction upon increased hydration. The layer-layer correlations of the ln q^2 vs. q^2 plots clearly indicate that the Ln ions remain associated with the clay, but the decrease in scattering intensity with absorption energy indicates that these ions apparently are not fully solvated within the interlayer. This latter result was not expected and there is speculation that these ions are instead associated as hydrolyzed species with the clay surface.

The pH of each metal ion-clay slurry during ion-exchange was monitored, and were well below the hydrolysis constants of the respective ion in every case (see Table I). It has been shown that at pH's above the pK_h values, Pb(II) and Cr(III) will form oxide-hydroxide precipitates on clay surfaces[10]. Below this critical pH, these ions simply exist as exchangeable cations within the interlayer. Cu(II) behaves in this manner.

Table I. Hydrolysis Study

ion-clay	pH during ion-exchange	pK_h[a]
Cu(II)	4.5	7.6
Er(III)	5.5	8.7
Yb(III)	5.5	8.0

[a]negative log of the hydrolysis constant[11].

Lanthanide ions appear to behave somewhat differently, however. Several years ago, a suite of articles reported how lanthanide sorption by montmorillonite was effected by pH, concentration, temperature, and pressure[12]. One finding reported that lanthanide hydrolysis occurs at lower pH values than are observed for aqueous solutions in the absence of clay[12c]. The presence of montmorillonite modifies the pH value at which the hydrolysis occurs, and "precipitation" commences at a lower value. This value was determined to be >5, which is in fact the case for our materials (pH 5.5). Hydrolysis is halted when the pH of the medium is acidified to <5. Er(III) and Yb(III) have similar ionic radii at 1.14 nm and 1.12 nm, respectively (coordination number 8)[11b]. Therefore, they likely have similar hydration energies and are expected to behave the same within the clay interlayer environment. It has been proposed that the specialized, localized electrostatic environment within a clay interlayer is strong enough to dissociate water ligands about a lanthanide ion, releasing OH- ions which then react to form hydroxides[12c].

The clay surface may have an even more active role, however. With large basal spacings (ca. 20 Å), hydrated ions experience an equipotential clay surface and can interact with the clay either through hydrogen bonding (complete hydration sphere) or direct residence on the interlayer surface (partial hydration sphere)[12b]. This latter state has been the one proposed for clay suspensions and pastes. In this case, hydrolysis involves dissociation of a coordinated water molecule followed by fixation of the metal ion to the clay. Sites available for this complexation are (1) the hexagonal holes created by the basal silicate surface and (2) other surface oxygen atoms. Both of these sites have been proposed to account for an adsorption of lanthanide ions in excess of that predicted by the cation exchange capacity[12b]. Our ASAXS results appear to support the view that the ions have indeed bonded to the silicate itself, rather than simply precipitate out separately as oxide-hydroxide phases on the surface.

CONCLUSIONS

We have demonstrated that the ASAXS effect can be observed in aluminosilicate clays containing 2-3 wt% transition metal and lanthanide ions. Further, that effect can be used to elucidate how the ions solvate when the clay is hydrated to form suspensions or pastes. For instance, Cu(II) solvates within the interlayer and therefore behaves as a mobile species capable of facile ion-exchange. Under similar conditions, ASAXS has also shown that some lanthanides (at least the smaller Er(III) and Yb(III) ions) will behave in an opposite manner and instead bind to the clay lattice. A thorough understanding of the kinetics and mechanisms of heavy metal ion sorption on clay mineral surfaces is a critical issue, and the subject of recent intensive study[13]. Our results will certainly add to the view of metal ion interactions at the clay-water interface.

ACKNOWLEDGEMENTS

This work was performed under the auspices of the U.S. Dept. of Energy, Office of Basic Energy Sciences, Divisions of Chemical Sciences and Materials Sciences, under contract no. W-31-109-ENG-38. Research at SSRL is supported by the Department of Energy, Office of Basic Energy Sciences. We thank H. Tsuruta for assistance with BL-4-2 at SSRL, and L. Xu (ANL) for assistance with XRD measurements.

REFERENCES

1. Grim, R. E. *Clay Mineralogy*; McGraw-Hill: NY, 2nd ed., 1953.
2. (a) Schobert, H. H. Coal: *The Energy Source of the Past and Future*, ACS: Washington, DC, 1987, p. 76 (b) Mraw, S. C.; De Neufville, J. P.; Freund H.; Baset Z.; Gorbaty, M. L.; Wright, F. J. in *Coal Science*, volume 2, Academic Press: NY, (Gorbaty, M. L.; Larsen, J. W.; Wender, I., Eds.), 1983, chap. 1.
3. Thiyagarajan, P.; Carrado, K.A.; Wasserman, S.R.; Song, K.; Winans, R.E. *Rev. Sci. Instrum.* **1996**, *67*(9), 1.
4. (a) Lyon, O. *J. Appl. Crystallogr.* **1985**, *18*, 480 (b) Miake-Lye, R. C.; Doniach, S.; Hodgson, K. O. *Biophys. J.* **1983**, *41*, 287 (c) Stuhrmann, H. B. and Notbohm, H. *Proc. Natl. Acad. Sci. USA* **1981**, *78*, 6216.
5. (a) Naudon, A. *NATO ASI Ser., Ser. C.* **1995**, *451*, 203 (b) Simon, J. P. and Lyon, O. in *Resonance Anomalous X-Ray Scattering*, North-Holland: Amsterdam, (Materlik, G.; Sparks, C.J.; Fischer, K., Eds.), 1994, 305-322.
6. Epperson, J. E. and Thiyagarajan, P. *J. App. Cryst.* **1988**, *21*, 652-662 and references therein.
7. (a) Haubold, H.-G.; Wang, X. H.; Jungbluth, H.; Goerigk, G.; Schilling, W. *J. Mol. Struct.* **1996**, *383*, 283 (b) Gerber, T. *J. Phys. IV* **1993**, *3*(C8, IX Int'l Conf. on Small Angle Scattering, 1993), 385.
8. Glatter, O. and Kratky, O. in *Small Angle X-ray Scattering*, Academic Press: NY, 1982.
9. Carrado, K. A. and Wasserman, S. R. *J. Am. Chem. Soc.* **1993**, *115*, 3394.
10. Gan, H.; Bailey, G. W.; Yu, Y. S. *Clays Clay Miner.* **1996**, *44*, 734.
11. (a) Baes, C. F. and Mesmer, R. E. *The Hydrolysis of Cations*, Wiley & Sons: NY, 1976 (b) Huheey, J. E. *Inorganic Chemistry*, Harper & Row: NY, 1978, p. 266.
12. (a) Miller, S. E.; Heath, G. H.; Gonzalez, R. D. *Clays Clay Miner.* **1983**, *31*, 17 (b) *ibid.* **1982**, *30*, 111 (c) Bruque, S.; Mozas, T.; Rodriguez, A. *Clay Minerals* **1980**, *15*, 413 (d) *ibid.* **1980**, *15*, 421.
13. (a) Stumm, W. *Chemistry of the Solid-Water Interface*, Wiley-Interscience: NY, 1992 (b) Scheidegger, A. M.; Lamble, G. M.; Sparks, D. L. *J. Coll. Interf. Sci.* **1997**, *186*, 118.

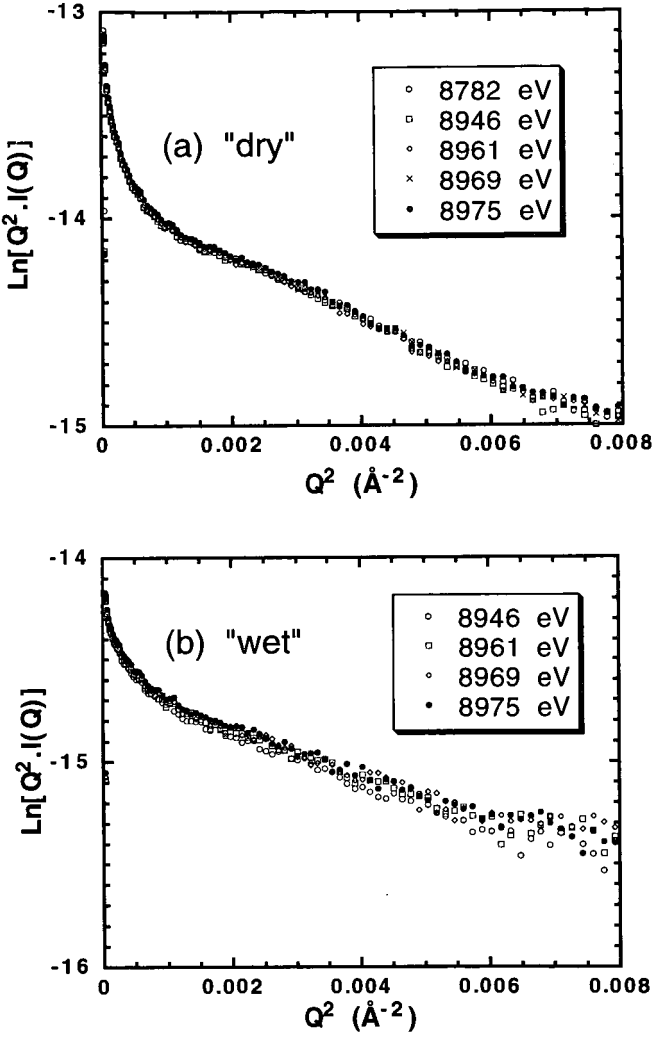

Figure 1. Modified Guinier sheet analysis of the ASAXS data for Cu(II)-clay as (a) the "dry" powder and (b) the "wet" paste.

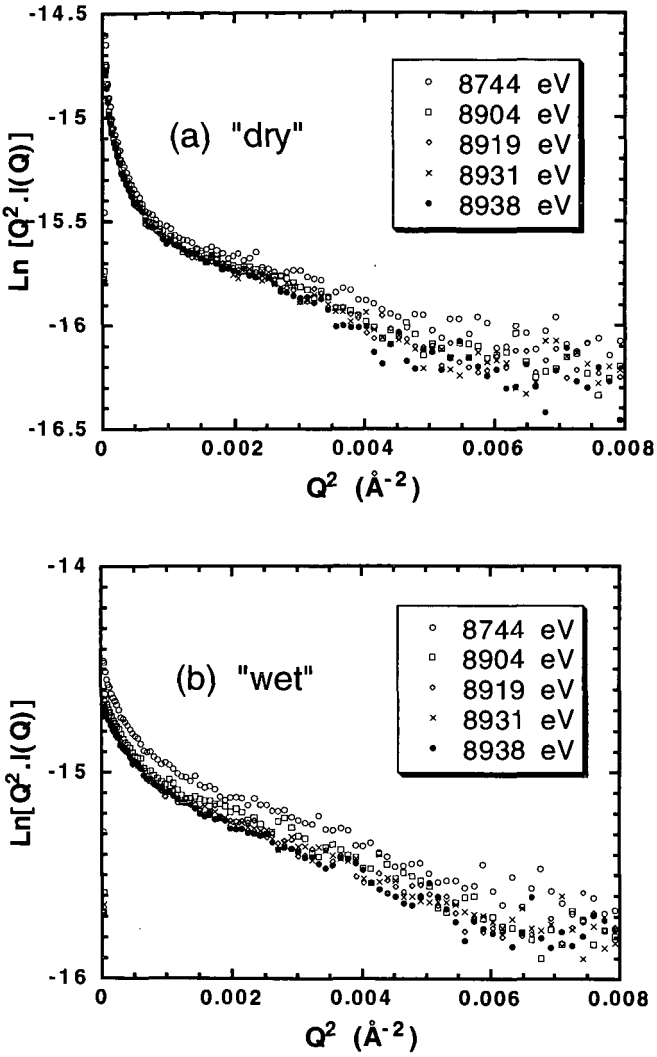

Figure 2. Modified Guinier sheet analysis of the ASAXS data for Yb(III)-clay as (a) the "dry" powder and (b) the "wet" paste.

SOLID STATE CARBON-13 NUCLEAR MAGNETIC RESONANCE STUDY OF AMORPHOUS AND CRYSTALLIZABLE PARAFFIN WAX FRACTIONS IN ASPHALT.

Laurent C. Michon, Daniel A. Netzel, and Thomas F. Turner
Western Research Institute, 365 North 9th Street, Laramie, Wyoming 82070, USA

Didier Martin and Jean-Pascal Planche
Centre de Recherche d'Elf Solaize, 6 Chemin du Canal, 69360 Solaize, France.

KEY WORDS

Solid State NMR, Wax, DSC

ABSTRACT

An asphalt cement is a viscoelastic material and as such its rheological properties are dependent on temperature. The temperature dependency of the rheological properties in turn can be attributed to the motion of the numerous chemical structures present in asphalt. With time, the molecular associations and the formation of crystalline structures tend to restrict molecular motion. Nuclear magnetic resonance is a powerful technique to record data on molecular motion. Solid state carbon-13 nuclear magnetic resonance measurements have been made at room temperature to characterize crystalline and amorphous methylene carbon atoms in asphalts. Cross-polarization with magic angle spinning experiments were performed on five asphalt samples with varying wax content. The amounts of amorphous and crystallizable methylene carbon atoms were determined using spectral deconvolution methodology and correlated with the wax content determined from differential scanning calorimeter measurements.

INTRODUCTION

Properties of asphalt cements are dependent on temperature and in a recent study, Lessueur *et al.* [1] have demonstrated that asphalt behaves like a Newtonian liquid between 60 to 180 °C, a viscolelastic material between the glass-transition temperature to 60 °C, and a rigid material below the glass-transition temperature. The temperature dependency of the asphalt properties can be attributed to the motion of its numerous chemical structures. At any given temperature, the extent of molecular motion depends on the intramolecular configuration of the various asphalt components and the manner in which they interact by intermolecular association. Among these components, the wax content in asphalt strongly influences asphalt properties.[2,3] In addition these wax components can produce crystalline material with time. The type and extent of molecular motion can be obtained from Solid-State carbon-13 Nuclear Magnetic Resonance (SS-NMR).[4,5] In these experiments variable contact time and dipolar dephasing sequences were conducted to obtain information on the crystalline and the amorphous aliphatic components in asphalt. Using the same type of methodology, it was interesting to see if SS-NMR measurements of the crystalline and amorphous components in asphalt are correlated to wax content determined using the Differential Scanning Calorimeter (DSC) measurements.

EXPERIMENTAL

Cross-Polarization with Magic Angle Spinning (CP/MAS) measurements were made using a Chemagnetics 100 solid-state nuclear magnetic resonance spectrometer operating at a carbon-13 frequency of 25 MHz. Experiments were conducted using a 7.5 mm rotor spinning at a rate of 4.5 kHz. Parameters included a pulse width of 5 μs, a pulse delay of 1 s, a contact time of 1 ms, a sweep width of 16 kHz, a free induction decay size of 1024 points, and 3600 acquisitions.

Conventional DSC measurements were performed on a TA instrument model 2920 Modulated DSC. After annealing, the sample was cooled at 10 °C/min to below 60 °C, held isothermally for 15 min, and then heated at 10 °C/min to the annealing temperature. The

different regions in thermogram were integrated with baseline correction. The energy associated with the melting endotherm was used to calculate the percentage of wax given in Table 1.

RESULTS AND DISCUSSION

Cross-polarization experiments were performed on five asphalts: A (Venezuelan crude), B (Middle East crude), C (Italian crude), D (African crude), and E (Middle East crude). These asphalts were provided by Elf-Antar France and were selected to have a large range in wax percentage (see Table 1). The NMR measurements were made at room temperature for the initial asphalt and after two months of phase evolution in the rotor. The aliphatic part of the spectrum was deconvoluted into fourteen different carbon types in accordance with the work of Netzel *et al.*[5] Figure 1 shows an example for asphalt D. The two peaks at 32 and 30 ppm correspond respectively to the crystalline methylene and to the amorphous methylene carbon atoms present in the paraffinic component of asphalt. The relative fraction for the two peaks (f CH_2-crys and f CH_2-amor) are given in Table 2. These values permit a calculation of the percentage of rigid (% C-rigid) and flexible (% C-flexible) carbon atoms (see Table 3) using the following expressions:

(% C-rigid) = (% C)(f C-aliph)(f CH_2-crys) and (% C-flexible) = (% C)(f C-aliph)(f CH_2-amor)

In these calculations, the % C is the percentage of total carbon atoms determined by elemental analysis and f C-aliph is the fraction of aliphatic carbon in the aromatic part of the ^{13}C SS-NMR spectrum.

After two months, an increase in the rigid carbon atoms content and, at the same time, a decrease in the flexible carbon atoms content were observed. This result suggest that, with time, crystalline materials are formed in a asphalt.

Most investigators report that the crystalline part of the asphalt corresponds to the wax fraction. Figure 2 shows the plot of the percentage of wax versus the percentage of rigid and flexible carbon atoms initially and after two months of phase evolution. The correlations obtained are relatively good (R^2 in the range 0.80 to 0.99). The high correlation suggests that the wax content of an asphalt is very well characterized by the two methylene carbon atom peaks at 32 and 30 ppm. The correlation is better with the amorphous part of the methylene carbon atoms because this part represents around 85 % of the total methylene carbon initially and 82 % after the two months of transformation.

CONCLUSIONS

Solid-state nuclear magnetic resonance spectroscopy appears to be a powerfull tool to study the crystalline and amorphous content of an asphalt. In this work, it has been demonstrated that the crystalline and the amorphous methylene carbon atoms present in an asphalt are correlated with the wax content.

REFERENCES

[1] Lessueur, D.; Gerard, J.-F.; Claudy, P.; Letoffe, J.-M.; Planche, J.P. and Martin, D., Journal of Rheology, *40*, 813, (1996).
[2] Claudy, P.; Letoffe, J.M.; Rondelez, F.; Germanaud, L.; King, G. and Planche, J.-P., Preprint Div. Fuel Chem. A.C.S., *37*, 1408, (1992).
[3] McKay, J.F.; Branthaver, J.F. and Robertson, R.E., Preprint Div. Fuel Chem. A.C.S., *40*, 794, (1995).
[4] Netzel, D.A.; Turner, T.F.; Miknis, F.P.; Soule, J. and Taylor, A.E., Preprint Div. Fuel Chem. A.C.S., *41*, 1260, (1996).
[5] Netzel, D.A.; Turner, T.F.; Forney, G.E. and Serres, M., Preprint Div. Polymer A.C.S., *38*, 829, (1997).

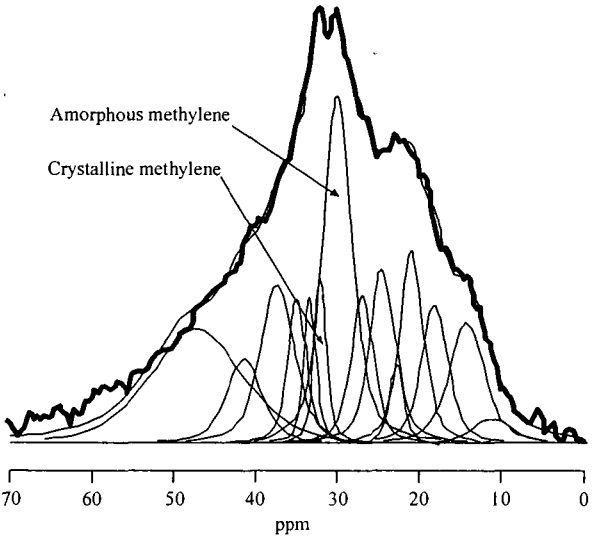

Figure 1: Deconvoluted ^{13}C NMR cross-polarization spectrum for asphalt D.

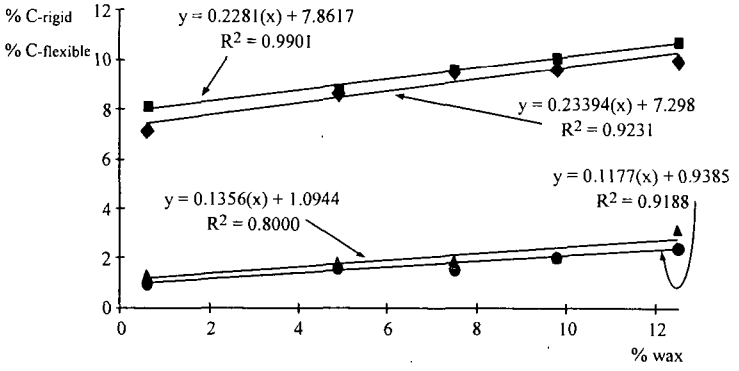

Figure 2: Correlation for the five asphalts between the percentage of wax and the percentage of rigid and flexible carbon atoms. The squares and the diamonds correspond to the flexible carbon atoms respectively initially and after two months of phase evolution. The circles and the triangles correspond to the rigid carbon atoms respectively initially and after two months of phase transformation.

Table 1: Percentage of wax determined by DSC measurements.

Asphalt	A	B	C	D	E
% of wax	0.60	4.90	7.50	9.80	12.50

on copper surfaces with relatively small amount of deposits produced on nickel and stainless steel surfaces. Large lumps of deposits seen as black spots in the micrograph for the copper deposits in Figure 1, did not give any C-H stretching bands, indicating that the deposit in these regions consisted mainly of solid carbon. An SEM examination of these lumps showed that they consisted of short fibers which were fused together[10]. The relatively thin layers of the deposits around the spotty deposits gave, however, distinctly different FTIR spectra with a strong aromatic C-H stretching band at 3050 cm^{-1}, as shown in Figure 1. The spectra obtained from these regions also showed aliphatic C-H stretching bands at 2955, 2925, and 2865 cm^{-1} attributed to CH_3 and CH_2 groups. These observations confirm the activity of the copper surface in catalyzing the formation of fibrous deposits from aromatic PAH produced during the pyrolysis of JP-8 jet fuel as proposed and discussed in more detail elsewhere[10].

The FTIR spectrum of the deposit found on the nickel coupon showed much less intense aromatic C-H band and more broad aliphatic C-H bands, as shown in Figure 1, compared to those obtained from the deposit on copper. A SEM examination of the nickel deposit did not show any filamentous carbon[10]. As different from copper and stainless steel coupons, the two sides of the nickel coupons appeared different under the microscope. The micrograph of the nickel surface in Figure 1 shows the more smooth side of the nickel foil with visible streaks; the other side appears to be more rough and grainy. No apparent difference was observed between the different sides of the coupons after stressing with the jet fuel, however, different deposition pattems were observed on the different sides of the nickel coupons during the pyrolysis of Norpar-13, as discussed later.

The deposits on the 304 stainless steel coupon gave a featureless spectrum, as shown in Figure 1, and no filamentous carbon was observed by SEM examination. The layers of deposits shown in the micrograph in Figure consist most likely of pyrolytic carbon.

The differences observed in the FTIR spectra of deposits on the three metal substrates indicate that the nature of the metal surface strongly affects the solid deposition from thermally stressed jet fuel. Both precursors to solids and the deposition mechanisms can be different on different metal surfaces.

Figure 2 shows the FTIR spectra and the micrographs of the deposits obtained on different sides of the nickel coupon from pyrolysis of Norpar-13 at 575°C and 500 psig in the flow reactor. Side A is the relatively smooth, and side B is the rough and grainy side of the coupons. Much heavier deposition was observed on the rough side of the coupon, as shown in the micrographs. The deposits on the rough side consisted mostly of filamentous carbon which gives the featureless spectrum in Figure 2. In contrast, the smooth side did not contain much filamentous carbon, seen as black spots on the micrograph, and the spectra obtained from regions other than the black spots gave relatively strong aliphatic C-H bands, as shown in Figure 2. The high activity of the rough surface for filamentous carbon formation can be explained with the relative ease of lifting metal particles from the surface in accordance with the mechanism proposed for filamentous carbon formation[11].

Figure 3 compares the FTIR spectra obtained from the deposits on the three metal coupons from pyrolysis of n-dodecane in a batch reactor at 450°C and 1500 psig for 3 and 5 hours. After 3 hours of reaction, the deposits on copper and nickel coupons gave stronger aromatic C-H bands than that seen from the 304 stainless steel deposits. There is not much difference in the spectra of the deposits on the different metal coupons after 5 hours of reaction. In all the cases, the aromatic C-H bands became more intense with time, indicating that the formation of aromatic compounds dominate the deposition process, as proposed earlier [5]. Under these conditions, incipient fibrous deposits were observed on the copper coupons, indicating, again, the catalytic activity of copper in producing fibrous carbon from aromatic compounds. Filamentous carbon was observed on the nickel coupon after 5 hours, suggesting that the precursors to filamentous carbon on the nickel surface are different from those leading to fibrous deposits on the copper surface. No filamentous carbon was observed on the 304 stainless steel coupon under the reaction conditions used for n-dodecane pyrolysis in the batch reactor.

ACKNOWLEDGMENTS

This work was supported by the US DOE Federal Energy Technology Center and the US Air Force Wright Laboratory/Aero Propulsion and Power Directorate, Wright-Patterson AFB. Funding was provided under contract DE-FG22-92PC92104. We thank Mr. W. E. Harrison III and Dr. T. Edwards of WL and Dr. S. Rogers of FETC for helpful discussions.

REFERENCES

1. Edwards, T. and Zabarnick, S. *Ind. Eng. Chem. Res.* **1993**, 32, 3117.
2. Edwards, T. and Atria, J. V., *ACS Preprints, Div. of Petrol. Chem.* ,**1995**, 40, 649.
3. Hazlett, R. N.; Hall, J. M.; and Matson, M. *Ind. Eng. Chem. Prod. Res. Dev.* **1977**, 16,171.
4. Eser, S. *Carbon* **1996**, 34, 539.
5. Song, C.; Eser, S.; Schobert, H. H.; and Hatcher, P. G. *Energy Fuels* **1993**, 7, 234.
6. Yu, J. and Eser, S. *Ind. Eng. Chem. Res.* **1996**, 36, 574.
7. Li, J. and Eser, S., *Extended Abstracts 22nd Biennial Conference on Carbon*, San Diego, CA (1995), p.314.
8. Edwards, T. *ACS Preprints, Div. of Petrol. Chem.*. **1996**, 41, 481.
9. Li, J. and Eser, S. *ACS Preprints, Div. of Petrol. Chem.* **1996**, 41, 508.

10. Li, J. and Eser, S., *Extended Abstracts 23rd Biennial Conference on Carbon*, University Park, PA (1997), in press.
11. Baker, R. T. K. and Harris, P. S., in *Chemistry and Physics of Carbon*, Edited by P. L. Walker, Jr. and P. A. Thrower, Vol. 14, Marcel and Dekker, New York, 1978, p. 83.

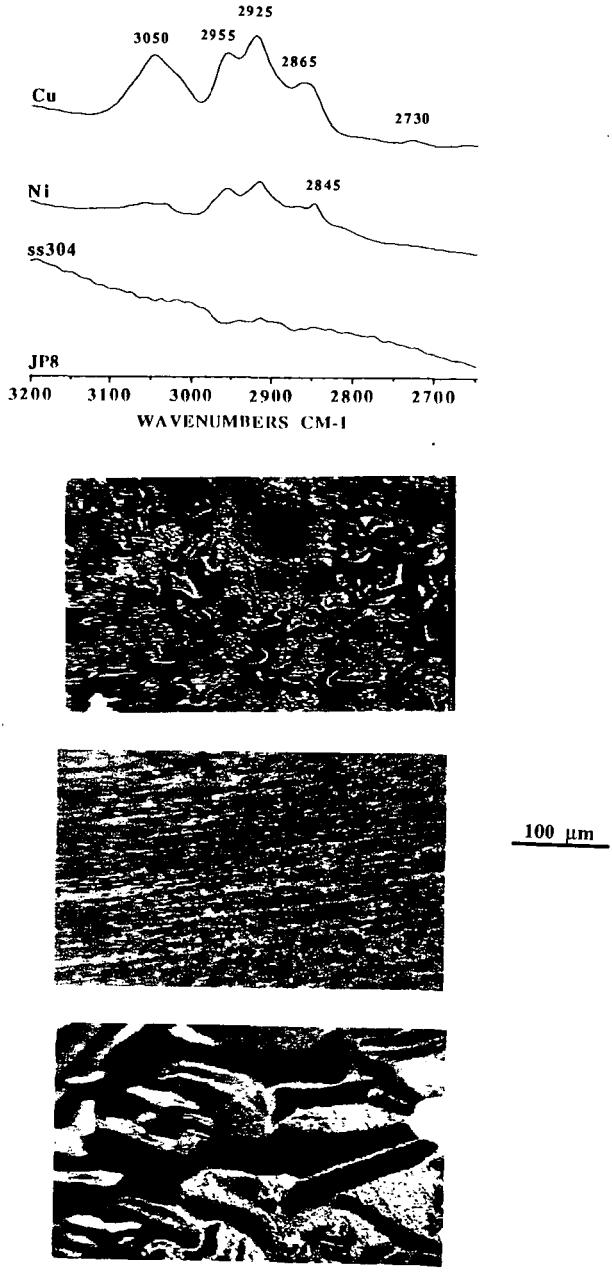

Figure 1. Micro FT-IR spectra and micrographs of solid deposits from JP-8 jet fuel on different metal substrates.

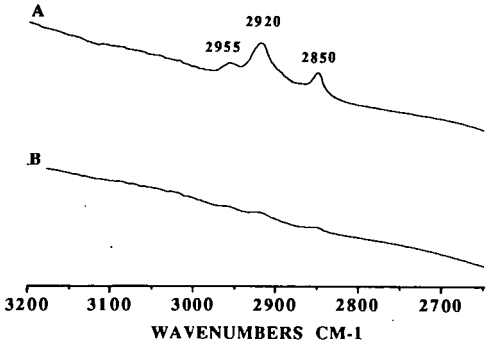

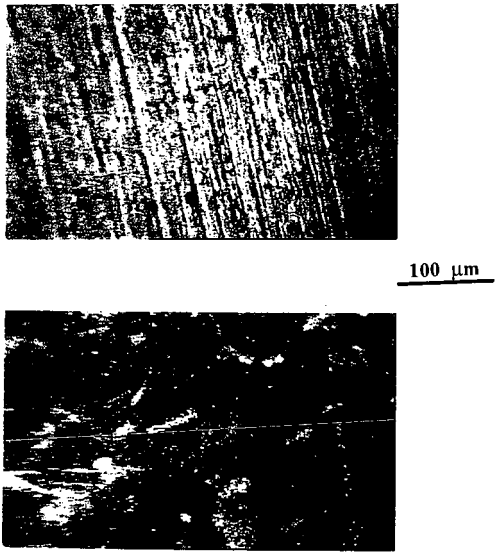

Figure 2. Micro FT-IR spectra and micrographs of solid deposits from Norpar-13 on different sides of a nickel foil: A: smooth side, B: rough side.

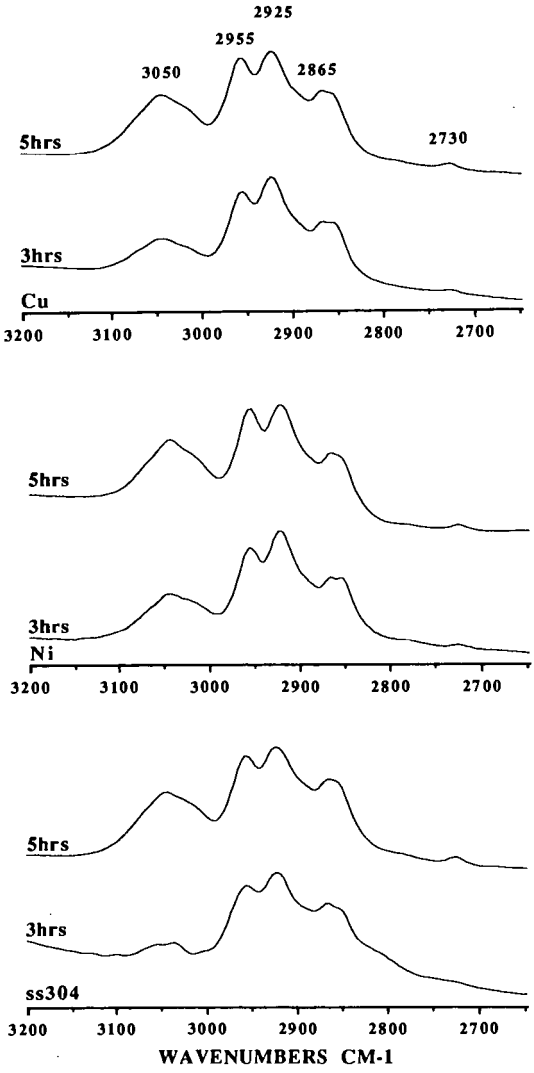

Figure 3. Micro FT-IR spectra of solid deposits from n-dodecane on different metal substrates as a function of time at 450°C.

SOME APPLICATIONS OF NUCLEAR MAGNETIC RESONANCE IMAGING TO RUBBER MODIFIED ASPHALTS

Francis P. Miknis and Laurent C. Michon
Western Research Institute
365 N. 9th Street
Laramie, WY 82070

Key Words: NMR imaging, asphalt, rubber

INTRODUCTION

In 1991, the United States Congress passed the Intermodal Surface Transportation Efficiency Act (ISTEA), which mandated the use of rubber from scrap tires in Federally funded roadway construction projects. The rationale for the mandate is easily understood when considering that the United States discards more than 300 million tires each year and that a large portion of these end up in stockpiles, which may create environmental problems and health hazards. Initially, the mandate called for 5% of scrap tire rubber to be used in 1992, increasing to 20 % by 1997. However, when the mandate was imposed systematic studies concerned with the effects of such variables as asphalt type, rubber type, particle size, mixing time and temperature on the asphalt-rubber rheological properties, as well as handling, safety and health effects of scrap tires had not been carried out. In 1995, the Federal mandate was lifted and States are no longer required by law to utilize scrap tires in paving projects. Nevertheless, between 1991 and 1995 systematic studies of various aspects of crumb rubber modified asphalts were made [1-5], and use of crumb rubber modified asphalts for paving has continued in California, Arizona and Florida.

Crumb rubber generally refers to scrap tires that are ground to a particle size of less than 4 mesh, although in the so-called "dry process" particle sizes of up to 12.5 mm might be used. Regardless of particle size, rubber tires are complex mixtures of elastomers (natural and synthetic rubber), curatives (sulfur, peroxides, etc.), cure-system activators (e.g., stearic acid), fillers and reinforcing agents (carbon black, fibers, etc.), process oils, plasticizer(s), and additives (antioxidants, antiozonents, etc.). Likewise, asphalts are complex mixtures of chemical compounds, consisting functionally of such compound classes as strong and weak acids, strong and weak bases, neutral (aromatic and aliphatic) compounds, and amphoterics. Therefore, questions about what happens when these complex materials are blended at mix temperatures (~170 °C) have not been satisfactorily answered. The influence of crumb rubber on rheology is somewhat understood [2], but the mechanisms of interaction of rubber and asphalt have been difficult to elucidate. For example, does the rubber dissolve in the asphalt, does it swell in the asphalt, do volatile components(extender oils, plasticizers) in the rubber migrate into the asphalt, and how might these reactions influence the rheological properties of the mixture? This work was undertaken to address some of these questions.

Although the crumb rubber mandate of ISTEA has been removed, there are enough successful applications of crumb rubber in asphalt to maintain an interest to more fully understand the compatibility and physicochemical interactions of these materials. This has been a difficult task because of the lack of suitable instrumental techniques to study these interactions. In this paper some preliminary results on the use of NMR imaging to study asphalt- rubber mixtures are presented. The results suggest that NMR imaging may provide a method to obtain information about asphalt-scrap tire rubber interactions. However, applications of NMR imaging to study asphalt behavior are still in their infancy [6,7].

EXPERIMENTAL

Sample Preparation. Natural tire rubber and styrene butadiene tire rubber samples were obtained from Rouse Rubber Industries, Inc. The natural rubber samples were roughly conical in shape (~8 mm dia x ~10 mm height) and sat on a circular base (16 mm dia x 2 mm height). The styrene-butadiene samples had the shape of a triangular prism (~16 mm base x ~8 mm height x ~1 0 mm length).

The natural rubber and styrene-butadiene samples were attached to the bottom of 23 mm (OD) glass vials with epoxy glue. This was to prevent their floating and moving during heating in the asphalt and to ensure that images taken after the heating experiments were made of the same sample orientation. The vials were then

placed in 25 mm(OD) flat-bottom glass tubes. The tubes were inserted into the MRI probe and were positioned in the probe using O rings such that the cross sections to be imaged were contained in the experimental field of view (FOV).

Two sets of samples were made for each rubber. One set was used for heating experiments in the absence of asphalt; the other set was used for heating experiments in the presence of asphalt. The asphalt chosen for study was derived from a crude oil from the San Joacquin valley, California and had a high carboxylic acid content (0.025 mol/l). Carboxylic acids have been shown to dissolve different rubber materials when heated to 200 °C for extended periods of time [2]. The asphalt was heated and then poured into the glass vials such that the rubber samples were several mm below the level of the asphalt.

Each sample was heated in an oven which was set at 170° C for periods of 1, 2, 4, 8, 12, 24 and 48 hours. Between the different heating periods, images were recorded while the sample cooled and after the sample was at room temperature. A temperature of 170 °C corresponds closely to the temperature at which the paving industry produces asphalt-rubber binders [3]. The temperature at which the images were acquired during the cooling phase was not known because the NMRI probe was not capable of variable temperature measurements. By convention, the samples were allowed to set for 3 minutes after they were removed from the oven. Images were then acquired using the same conditions described below, except only 2 acquisitions were obtained.

NMR Imaging Experiments. NMR imaging experiments were carried out at a nominal proton resonance frequency of 200 MHz using a Chemagnetics/Otsuka Electronics microimaging probe. For elastomeric and viscous materials, the relaxation times of the protons are generally too short for spin echo imaging. Consequently, a 3D imaging technique was used.

Images using the 3D method were acquired using an echo time of 2 ms, a pulse delay of 0.5 s, a free induction decay size of 256 data points, 64 phase encodes, 20 acquisitions and a gradient strength of 70 G/cm. Eight 3 mm thick slices were obtained in a FOV of 22 mm. The measuring time was ~1.4 hrs for these experiments. Images taken during cooling were acquired under the same conditions, except that 2 acquisitions were made. These images were acquired in ~8.5 minutes. All images were recorded in the XZ plane, where the z axis is the direction of the magnetic field and also corresponds to the cylindrical axis of the glass vial.

RESULTS AND DISCUSSION

Images of natural tire rubber (Figure 1) and styrene butadiene tire rubber (Figure 2) in the absence and presence of asphalt were acquired before and after heating, and during cooling using the 3D technique. NMR images of the protons in asphalt are not obtained at room temperature because the lack of molecular mobility (high viscosity) shortens the NMR relaxation times such that the NMR signal decays away before any spin echoes can be formed. Only the protons in the rubber are imaged at room temperature. However, at higher temperature the NMR relaxation times are lengthened so that asphalt protons that do not image at room temperature might be imaged at the higher temperature. In the lower sets of images in Figures 1 and 2, signals from the heated asphalt can be seen as the light contrast surrounding the rubber samples. In the bottom set of images in Figure 2 b- d, the signal (light area) below the triangularly shaped styrene-butadiene is an artefact. In reality, this signal is the top of the asphalt covering the rubber, but has been folded into the image because the positioning of the sample in the image probe was such that the field of view (FOV) was not large enough to encompass the sample. In all cases, the 5th slice of an image set of 8 slices is shown. This slice is a 3 mm thick slice through the approximate center of the sample in the XZ plane.

In Figure 1, the set of 4 images at the top are for the natural tire rubber heated at 170 °C for 0 (unheated), 2, 8, and 24 hrs in the absence of asphalt. The middle set of 4 images are for another natural tire rubber sample heated for the same time periods, but in the presence of asphalt. These images were recorded when the sample returned to room temperature after having been heated at 170 °C for the different periods of time. The bottom set of 4 images was acquired while the sample was cooling to room temperature. Analogous sets of images were acquired for styrene-butadiene crumb rubber heated in the same manner and are shown in Figure 2.

The intensity of the NMR images decreases with increased time of heating. This is true for both the natural tire rubber and styrene-butadiene tire rubber, heated in the presence and absence of asphalt (Figures 1 and 2, top and middle). The loss of signal

is more evident for the rubber pieces that were heated in asphalt, and more so for styrene-butadiene compared to natural rubber.

From an NMR perspective, the loss of signal intensity could have different origins: The rubber could have become more rigid in the asphalt and as a result, the relaxation times would have become shorter. This could happen, for example, if oils and plasticizers were driven from the rubber and/or cross linking reactions occurred as a result of heating.

Another reason for the loss of signal intensity could be that the rubber had dissolved in the asphalt, and the only signal remaining was due to the undissolved material. Others [2,3] have shown that, depending on asphalt crude oil source, crumb rubber particles dissolve in asphalt when heated at elevated temperatures (170 - 200 °C) for extended periods of time.

Natural rubber and styrene-butadiene rubber samples that were heated in the absence of asphalt had undergone changes in structure and became more rigid. This was apparent both from the hardness of the rubber samples after heating, and the fact that the rubber samples were impervious to solvents, such as chloroform, after heating (i.e., did not swell). The apparent change in the physical state of the rubber could be due to oxidation at the rubber surface and/or devolatilization and cross linking reactions in the rubber. Loss of the extender oils could also account for some of the rigidity and brittleness exhibited by the rubber samples after heating in the absence of asphalt. Thermal gravimmetric analysis data show that loss of volatile matter in elastomers begins at temperatures around 100 °C [8]. Thus, heating the samples at 170 °C for extended periods of time, as was done in this study, could lead to loss of volatile matter.

The real effect on the tire rubber samples when heated in the presence of asphalt is betrayed by the lower sets of 4 images in Figures 1 and 2. These images were acquired during cooling and clearly show that the rubber had swelled substantially with no evidence of dissolution. However, because the experiments were conducted using large pieces of rubber to enhance the NMR image signal intensity, observation of the swelling behavior would be enhanced over any dissolution that may have taken place. In fact, the cross-section of the natural tire rubber had swelled to about 1.6 times its normal size and the edges did not show any discernible deterioration as would be expected if dissolution had occurred. The images of the swollen rubber could be reproduced by simply reheating the sample for 10 minutes after it had been at room temperature and re-imaging the sample. These images indicate that the loss of signal in the middle sets of images is not due to dissolution of the rubber. However, these images were acquired on rubber pieces that are large compared to crumb rubber particles used in paving, which are typically 4 mesh or less. Therefore, whether dissolution would occur for finer rubber particles mixed in asphalt cannot be ruled out based on these results. Others [2,3] have observed dissolution of fine particles of rubber when heated in asphalt. The images of the swollen rubber also negate the notion that the rubber had crosslinked and became more rigid when heated in the asphalt.

There was little or no swelling of the rubber samples when heated in the absence of asphalt. This is seen by the top set of images in Figures 1 and 2. The lack of swelling was also verified visually immediately after the samples were removed from the oven. Thus, the swelling of the rubber in asphalt appears to have been caused by solvent penetration of components in the asphalt, possibly maltenes. Valkering et al.[9] have shown that maltenes from asphalt cause considerable swelling in styrene-butadiene- styrene block copolymer/asphalt blends. In addition, oils used in tire manufacture are similar to compounds found in neat asphalts. During heating, interaction and/or exchange of these oils with oils in the asphalt could account for the swelling of the rubber. This exchange might also account for the loss of signal at room temperature if the relaxation times of the rubbers took on those of the asphalt components.

SUMMARY

Applications of NMR imaging to study polymer modified asphalts are in their infancy. In this study, exploratory NMR images were acquired on large pieces of natural and styrene-butadiene tire rubbers soaked in asphalt. These measurements demonstrated the feasibility of using NMR imaging to study different interactions between tire rubbers and asphalt, such as swelling by asphalt molecules, possible dissolution of rubber components in asphalt, and devolatilization and cross-linking in rubber when heated at mix temperatures of 170 °C.

Observation of swelling of crumb rubber in asphalt has been extremely difficult, but these results clearly show that swelling of tire rubber in asphalt is a significant mechanism in crumb rubber modification of asphalt, at least for larger pieces of rubber.

DISCLAIMER

ACKNOWLEDGMENTS

The authors gratefully acknowledge support of this work by the Federal Highway Administration under Contract No. DTFH61-92-C-00170. One of the authors, L.C.M., gratefully acknowledges Elf-Antar, France, for financial support.

REFERENCES

1. Labib, M. E., Memon, G. M. and Chollar, B. H., *Prepr..Pap.-Amer. Chem. Soc. Div. Fuel Chem.*, 1996, **41(4)**, 1209.

2. Tauer, J. E. and Robertson, R. E., *Prepr. Pap.-Am. Chem. Soc. Div. Fuel Chem.*, 1996, **41(4)**, 1214.

3. Billiter, T. C., Chun, J. S., Davison, R. R., Glover, C. J. and Bullin, J., *Prepr. Pap.-Am. Chem. Soc. Div. Fuel Chem*, 1996, **41(4)**, 1221.

4. Shih, C.-T., Tia, M. and Ruth, B. E., *Prepr. Pap.-Am. Chem. Soc. Div. Fuel Chem.*, 1996, **41(4)**, 1227.

5. Coomarasamy, A., Manolis, S. and Hesp, S., *Prepr. Pap.-Am. Chem. Soc. Div. Fuel Chem.*, 1996, **41(4)**, 1322.

6. Miknis, F. P. and Netzel, D. A., *Prepr. Pap.-Am. Chem. Soc., Div. Fuel Chem.*, 1996, **41(4)**, 1327.

7. Miknis, F. P. and Pauli, A. T., *Prepr. Pap.-Am. Chem. Soc., Div. Fuel Chem*, 1997, **42(2)**, 374.

8. Sircar, A. K., *Thermal Characterization of Polymeric Materials.*, Academic Press In, New York, 1997, 888.

9. Valkering, C. P., Wonk, W. C. and Whiteoak, C. D., *Shell Bitumen Review*, 66, May 1992, 9-11.

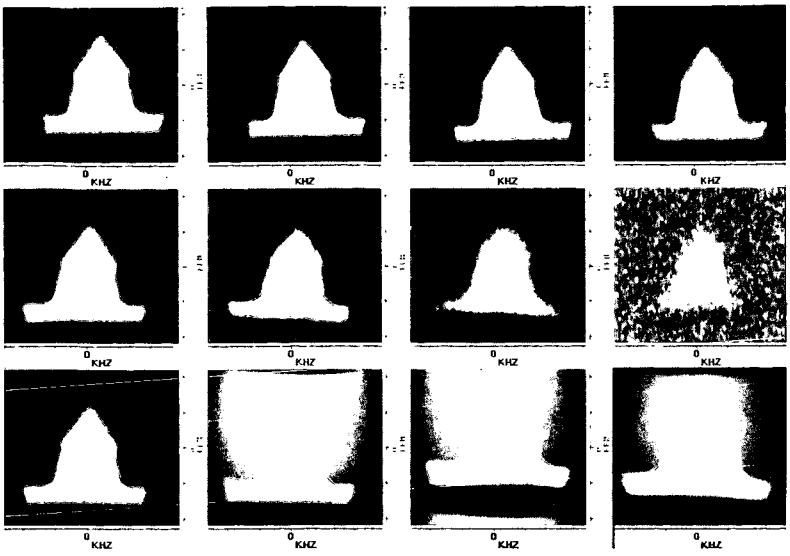

Figure 1. NMR images showing the cross section of a conical piece of natural tire rubber taken after heating at 170 °C for (a): 0, (b) 2, (c) 8, and (d) 24 hrs. (top) natural tire rubber heated in the absence of asphalt; (middle) natural tire rubber heated in the presence of asphalt. Both sets of 4 images were acquired when the sample was at room temperature. (bottom) natural tire rubber heated in the presence of asphalt and imaged while the sample cooled to room temperature.

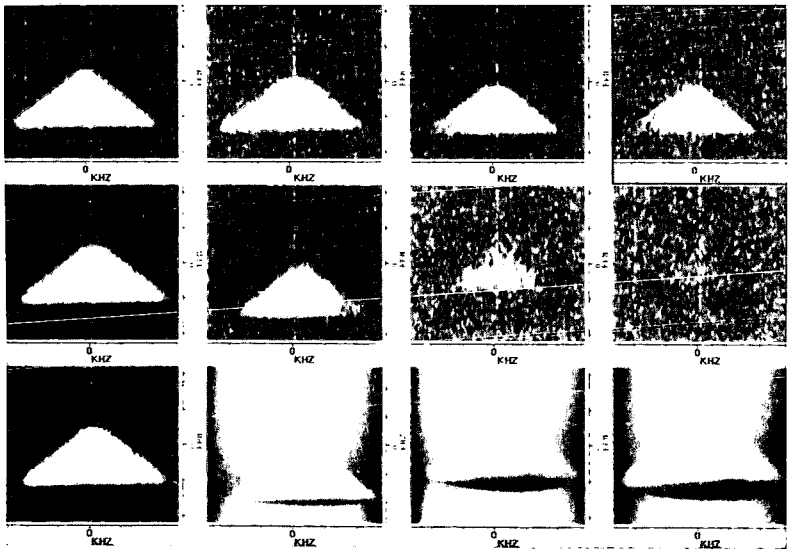

Figure 2. NMR images showing the cross section of a triangular prism-shaped piece of styrene-butadiene tire rubber taken after heating at 170 °C for (a): 0, (b) 2, (c) 8, and (d) 24 hrs. (top) styrene-butadiene tire rubber heated in the absence of asphalt; (middle) styrene-butadiene tire rubber heated in the presence of asphalt. Both sets of 4 images were acquired when the sample was at room temperature. (bottom) styrene-butadiene tire rubber heated in the presence of asphalt and imaged while the sample cooled to room temperature.

DIGITAL IMAGE ANALYSIS OF OPTICAL TEXTURE AND POROSITY OF PETROLEUM COKES

Gao Lin Qiao and Semih Eser
Fuel Science Program
Department of Materials Science & Engineering
209 Academic Projects Building
The Pennsylvania State University, University Park, PA 16802, USA

INTRODUCTION

The microstructure of coke particles can be considered to consist of their optical texture and porosity[1]. Optical texture refers to the appearance of the surface under a polarized-light microscope. The size and shape of isochromatic areas observed on polished surfaces can be used to identify different types of texture[2]. Characterization of the optical texture is very difficult, since the optical domains in petroleum cokes are often connected and tortuous. Several image analysis techniques have been used to determine the size, shape, and orientation of the optical domains in calcined petroleum cokes[3-6]. For texture analysis of calcined cokes, the pores are either ignored[4], or masked out by image processing[3]. In the present study, we propose a digital analysis method to simultaneously characterize the texture and porosity of the calcined cokes. An image analysis method was developed to extract the boundaries of optical domains and pores in petroleum cokes. For semi-cokes, only the boundaries of optical domains were extracted to characterize the optical texture. For calcined cokes, the boundaries of the optical domains and the pores were used to characterize the microstructure of the samples. Feature indices were defined and calculated based on the shape and orientation of the extracted boundaries for the optical domains and pores. Before image analysis, thermal expansion measurements were carried out on the same calcined coke particles to see if there is any relationship between the feature indices and the thermal expansion coefficients (CTE) of calcined coke samples. The CTE is one of the critically important properties of the calcined needle cokes used for manufacturing graphite electrodes for electric-arc furnaces[7].

IMAGE PROCESSING TECHNIQUES

It is well known that there are no distinct gray levels which separate two different isochromatic regions in a polarized-light image of an anisotropic carbon[3]. Therefore, one cannot readily identify the boundaries of these isochromatic regions. It is, however, possible to use a local derivative operator to extract the boundaries of different objects in a given image. For example, the Robert's cross operator[8] acts on a 3x3 pixel region of an image (the z's are gray levels), using the two arrays shown below to obtain a new gray level at point z_5 as $|(z_1+z_3)-(z_7+z_9)|+|(z_3+z_9)-(z_1+z_7)|$.

z_1	z_2	z_3
z_4	z_5	z_6
z_7	z_8	z_9

1	0	1
0	0	0
-1	0	-1

-1	0	1
0	0	0
-1	0	1

These operators are adopted to detect the edges and to draw the boundaries of the objects. using horizontal and vertical gradients. Figure 1 shows different images of a domain structure in a semi-coke sample, including a gray level image (a), boundary image (b), and a binary boundary image (c), created by image processing techniques. As seen Figure 1(a), interpreting optical domains as objects would give complex object shapes. In many cases, an optical domain is not an enclosed object. Therefore, instead of analyzing the complex shapes of optical domains directly, one can analyze the boundaries of these optical domains. The boundary image shown in Figure 1(b) was created by the Robert's cross operator. Although the boundary image does not exactly reflect the shape and size of the optical domains it preserve many features of the optical domains from which it was derived.

After a boundary image is created, it is necessary to expand the gray levels of boundary image to the whole gray scale (0=black, 245=white) by using the stretching technique[8], since the gray levels of the boundary image occur only at the dark end of the gray scale. The stretching technique is used to increase the contrast of the image. Figure 2 shows the linear operation of contrast transformations. After stretching the gray levels of the boundary image shown in Figure 1(b), a threshold of gray level 67 was chosen to obtain the binary image shown in Figure 1(c). Only binary images can be used for feature analysis.

EXPERIMENTAL

Both commercial calcined needle coke samples and semi-coke samples produced in the laboratory were used for image analysis. Thirteen semi-coke samples were prepared by carbonizing commercial coker feedstocks in closed tubing reactors at 500°C for 3h. Before carbonization, 4 g of each sample was weighed in an aluminum foil tube and then placed in the stainless steel reactor. After carbonization, the resultant lump coke was mounted in an epoxy resin

pellet longitudinally. Polished pellets of semi-coke samples were placed on the microscope stage such that the long axis of the coke samples was parallel to the x-axis of the stage.

Before the calcined coke particles were examined under the microscope, thermal expansion measurements were performed in an ORTON 1600D dilatometer. Nine particles were picked from four calcined coke samples and cut into cylinders of approximately 2.50 cm in length and 0.75 - 1.00 cm in diameter. The particles were cut such that their apparent long dimension was parallel to the long axis of the cylinders. For CTE measurements, samples were heated at a rate of 3°C/min in an argon atmosphere and linear changes of samples were recorded from room temperature to 800°C. For comparison with the published literature[3,5], the CTE values were calculated for the same temperature range (300-700°C) for all the particles. When three replicate measurements were performed on each sample, the results showed a standard deviation of 1-2%. After CTE measurement, the samples were placed longitudinally in epoxy resin blocks to prepare polished pellets for microscopic examination.

Image acquisition from a polarized-light microscope (Nikon, Microphot-FXA) was carried out via a high resolution video camera and an image analysis system (PGT, IMAGIST)[9]. After the binary image was created from the boundary image as described in the previous section, it was used for feature analysis[10]. Usually, thirty images were analyzed for each pellet. Only the features in the size range of 50 μm^2 and 1500 μm^2 were analyzed to exclude large cracks and polishing artifacts from the measurements.

A manual point counting technique was also used to characterize the semi-coke samples to compare the results with those obtained by digital image analysis. An automated microscope stage was used to scan the sample by moving a mask of 1mmx1mm on each pellet[8].

RESULTS AND DISCUSSION

For feature analysis of the binary boundary image, we used three parameters, longest dimension (LD), breadth(B), and horizontal chord (HC). Using these three parameters, a feature Index, called FRI, was defined to reflect the shape and orientation of the boundaries of optical domains. The following equation was used to calculate the feature indices for each pellet:

$$FRI = (1/n)\sum^{n}((\sum_{j=1}^{m}\frac{LD_j}{B_j}\times HC_j)/m) \qquad (1)$$

where: m is the number of features in an image; n is the number of images (normally, n=30). Cokes with more anisotropic and well oriented structures should have higher values of feature index. Using a semi-automated point counting data and the assigned factors for four texture classifications, another optical texture index (OTI) was calculated as described before[8].

Figure 3 shows a plot of feature index (FRI) against optical texture index (OTI) for semi-coke samples. It appears that the boundary analysis of optical domains can represent the characteristics of the optical texture of semi-cokes. Unlike point counting, the boundary analysis method does not require texture identification for each image. Instead of analyzing the complex shape of the optical domains, the method relies on the boundary properties of the texture domains.

Figure 4 shows a gray level image (left) and a binary boundary image (right) of a calcined coke sample with a highly anisotropic needle coke texture. The comparison of the two images shows that the extracted boundaries represent both the texture domains and the pores seen in the gray level image. It can also be seen that there is a close correspondence between the boundaries of the texture domains and the pores. For feature analysis of the boundary image, an area exclusion formula was used to remove the large cracks (>1500 μm^2) and small pores (< 50 μm^2). From the feature analysis, a feature index (FRI) of 106 was calculated by Equation 1, which reflects the highly anisotropic microstructure of the needle coke image.

In comparison, Figure 5 shows images of a less anisotropic calcined coke sample, with much smaller sizes of optical texture elements and more isometric boundaries of the pores. The feature analysis of the binary boundary image gave a much smaller FRI (25) compared to that obtained for the highly anisotropic needle coke structure shown in Figure 4 (106). These examples show that FRI calculated from the boundary images of the texture domains and pores in the calcined cokes provides a measure of the degree of miscrostructural anisotropy.

Figure 6 shows a plot of the coefficient of thermal expansion (CTE) against the calculated feature index of the nine calcined coke particles. The plot shows that there is a good correlation between the CTE and FRI within a narrow range of low CTE values desired for the needle cokes used for manufacturing graphite electrodes. This sensitive relationship between the CTE and FRI suggests that the characteristics of both the optical texture and the pores which have the similar size range of optical texture can affect the CTE of calcined cokes [11]. The apparent close correspondence between the optical texture and the pore structure can be explained by considering that the pores analyzed in this study were produced most likely by shrinkage during calcination[7].

CONCLUSIONS

Boundary imaging and analysis can be used to characterize the microstructure of semi-cokes and calcined cokes in terms of a feature index, A feature index was defined to represent the size, shape, and orientation of the optical domains obtained by polarized-light microscopy and digital image processing. The principal advantage of this technique is that there is no need to identify the individual texture elements in a given image. A good correlation was observed between the thermal expansion coefficients of the calcined cokes and feature indices derived by digital image

analysis of the optical texture and pore structure. For feature analysis, there is no need to exclude the pores which have a comparable size range to that of the texture elements.

ACKNOWLEDGMENTS

This study was supported by the Carbon Research Center at the Pennsylvania State University, and Conoco, Inc. We thank Dr. Robert E. Miller of UNOCAL Corporation and Dr. Bruce E. Newman and Dr. Walter A. Kalback of Conoco, Inc. for helpful discussions and thank Ronald M. Copenhaver for polishing the optical pellets and assembling the tubing reactors.

REFERENCES

1. Eser, S. and Hou, L., *Carbon* **1996**, 34, 805.
2. Edwards, I. A. S., in *Introduction to Carbon Science*, Edited by H. Marsh, Butterworths, London, 1989, p.20.
3. Eilersten, J. L., Rrvik, S., Foosns, T., and Øye, H.A., *Carbon* **1996**, 34, 375.
4. Mochida, I., Korai, Y., and Oyama, T., *Carbon* **1987**, 25, 273.
5. Eilersten, J. L., Hole, M., Foosns, T., and Øye, H.A., *Extended Abstracts, 21st Biennial Conf. on Carbon*, Buffalo, New York (1993), p. 675.
6. Lewis, R. T., Lewis, I. C., Greinke, R.A. and Stong, S.L., *Carbon* **1987**, 25, 289.
7. Mochida, I. Fujimoto, K. and Oyama, T. In *Chemistry and Physics of Carbon* (Edited by P.A. Thrower), Vol. 24, pp. 111-212, Marcel Dekker, New York, 1994.
8. Gonzalez, R. C. and Words, R. E., in *Digital Image Processing*, Addison-Wesley, Reading, Mass., 1992.
9. Qiao, G. L., Wang, Y., Zeng, S. M. and Eser, S., *Proceedings of the European Carbon Conference Carbon'96* , Newcastle, UK (1996), p.176.
10. Qiao, G. L. and Eser, S., *Extended Abstracts, 23rd Biennial Conf. on Carbon*, University Park, Pennsylvania, (1997).
11. Kakuta, M., Tanaka, H., Sato, J., and Noguchi, K., *Carbon* **1981**, 19, 347.

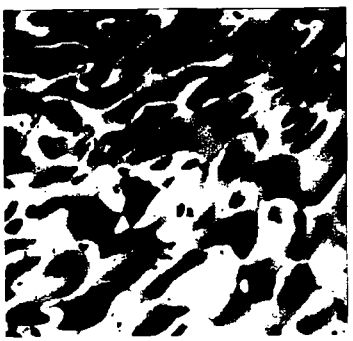

100 μm

(a)

(b)

(c)

Figure 1. Typical images of domain structure in semi-cokes: (a) gray level image; (b) boundary image; (c) binary boundary image.

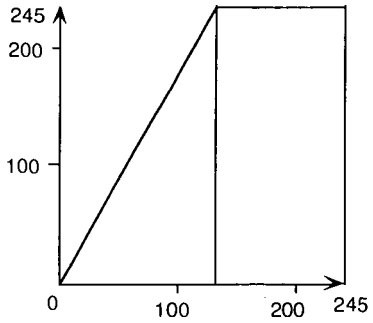

Figure 2. The linear form of transformation function used in contrast stretching.

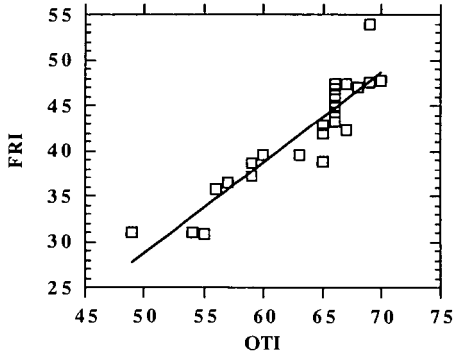

Figure 3. Comparison of feature index (FRI) with optical texture index (OTI).

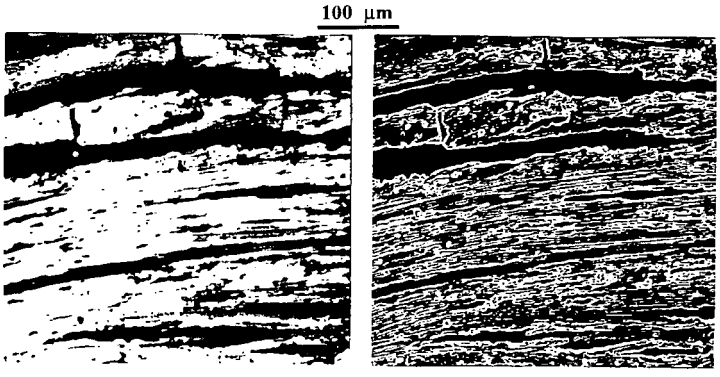

Figure 4. The images of calcined cokes with needle structure; gray level image (left), binary image (right), FRI = 106.

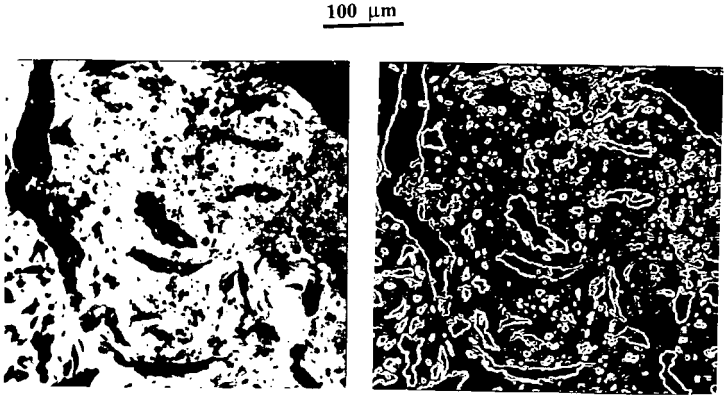

Figure 5. The images of calcined cokes with small domain structure; gray level image (left), binary image (right), FRI = 25.

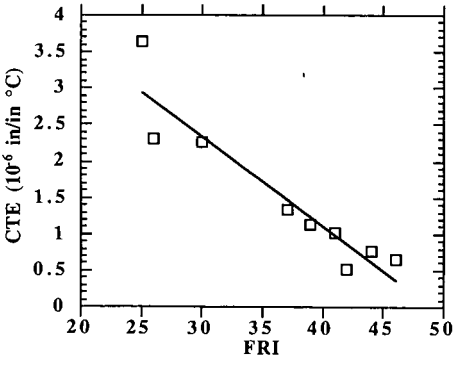

Figure 6. The relationship between coefficient of thermal expansion (CTE) and feature index (FRI) of calcined cokes.

APPLICATION OF ISOTOPE-RATIO-MONITORING GAS CHROMATOGRAPHY/MASS SPECTROMETRY TO STUDY CARBONIZATION REACTIONS OF FCCU SLURRY OILS

T. R. Filley, R. M. Filley*, S. Eser*, and K. H. Freeman, Department of Geosciences
*Department of Materials Science and Engineering, The Pennsylvania State University
University Park, PA 16802

ABSTRACT

Delayed coking of Fluid Catalytic Cracking Unit (FCCU) slurry oils produces needle cokes which are used in the manufacture of graphite electrodes for electric-arc furnaces. The structure and properties of needle cokes depend on the formation of a liquid crystalline phase (carbonaceous mesophase) during delayed coking. Thermal reactivity of individual compounds in slurry oils effectively controls the initial carbonization reactions, and, thus, the degree of mesophase development. In this study, isotope-ratio-monitoring gas chromatography mass-spectrometry was used *in conjunction with* a ^{13}C-labeled dopant (4-methyldibenzothiophene) to determine the distribution of the labeled methyl group on the GC-amenable products from carbonization of three different FCCU slurry oils. Selective removal of the unreacted dopant and its methylated analogs from the reaction products by ligand exchange chromatography allowed the isotope analyses of selected aromatic compounds. The ^{13}C enrichment of selected aromatic compounds, including some isomers, was determined to compare the relative thermal reactivities of different compounds as well as the reactivities of different sites on a given aromatic compound.

INTRODUCTION

The complex chemical constitution of fossil fuels and many associated refinery products precludes the use of simple chromatographic or bulk spectroscopic analytical techniques to accurately evaluate reaction mechanisms and rates of thermal and catalytic conversion of individual compounds. A relatively recent approach to studying the reactivity of individual compounds within complex organic mixtures combines the addition of organic compounds or gaseous media enriched in stable isotopes that participate in alkylation/dealkylation and/or hydrogen abstraction/addition reactions. The rationale for this approach is that the labeled compound or atom can be accurately tracked though a reaction sequence by the use of instrumentation such as, NMR, high resolution mass spectrometry, and isotope-ratio-monitoring gas chromatography mass-spectrometry (irmGCMS). Valuable insights into complex reactions in resid/coal coprocessing[1], crude oil maturation[2], jet fuel thermal stability[3] and the carbonization of FCCU slurry oils[4,5] have been obtained by this application.

In a previous publication, (Filley et al.[4]), we reported the results from irmGCMS of the reaction products from the carbonization of an FCCU slurry oil (referred to in this paper as Oil A) and 4-methyldibenzothiophene, ^{13}C-labeled at the methyl carbon (4-^{13}MDBT). We observed the progressive ^{13}C-enrichment of methylated PAH within the reaction products during the course of the reaction indicating that ^{13}C-enriched methyl radicals were formed by thermolysis of the labeled methyl group and dibenzothiophene. The reactivity of specific methyl substituted and unsubstituted PAH toward reaction with the ^{13}C-enriched methyl carbon were documented. Filley et al.[4] observed that the relative enrichment in ^{13}C between structural isomers of specific methyl PAH could be explained based upon calculated reactivities from free valence indices. In this report we present the irmGCMS analysis of the carbonization products of two additional FCCU slurry oils (Oil B and Oil C) with 4-^{13}MDBT to compare the relative reactivities of specific PAH toward reaction with the ^{13}C-enriched methyl radicals.

EXPERIMENTAL

The FCCU slurry oils were carbonized (500 °C) in closed tubing bomb reactors with 2 wt% 4-methyldibenzothiophene, ^{13}C-labeled at the methyl substituent. Reaction conditions, product extraction and molecular quantification were described in Filley and Eser[5]. The carbon isotopic compositions of individual compounds were determined by isotope-ratio-monitoring gas chromatography-mass spectrometry.[6-8] The irmGCMS system used in this study consists of a Varian model 3400 GC coupled to a Finnigan MAT 252 isotope-ratio-monitoring mass spectrometer by a micro-volume combustion furnace. A fused silica capillary chromatographic column (25 m x 0.32 mm i.d. DB-5MS with 0.5 μm film thickness) was used with helium as a carrier gas. As the compounds elute from the gas chromatograph they are quantitatively combusted to CO_2 and H_2O within the combustion furnace (Cu:Pt, 2:1 maintained at 850°C). Masses 44 ($^{12}C^{16}O_2$), 45 ($^{13}C^{16}O_2$, $^{12}C^{17}O^{16}O$) and 46 ($^{12}C^{18}O^{16}O$) are simultaneously monitored. The isotopic compositions of individual compounds were determined by comparison to reference CO_2 gas calibrated relative to NBS-19 standard. Isotopic compositions are reported relative to the international standard, Pee Dee Belemnite (PDB) in delta ($\delta^{13}C$) notation as described in the following equations.

$$\delta^{13}C(‰) = [(R_{sa} - R_{st}) / R_{st}] \times 1000$$

where:

R_{st} = the isotopic ratio $^{13}C/^{12}C$ of PDB standard (0.011237)
R_{sa} = the isotopic ratio $^{13}C/^{12}C$ of the sample compound

The values measured by irmGCMS represent the average isotopic composition of all carbon atoms in the molecule. The ^{13}C-enriched carbon is associated only with the methyl groups on the substituted PAH[4]. Therefore, the isotopic enrichment of the methyl carbons associated with monomethyl substituted PAH was calculated with a mass balance expression. The isotopic enrichment of the methyl group, expressed as $\Delta\delta^{13}C_m$, is determined by difference between the $\delta^{13}C$ of the methyl substituent on the methyl PAH produced in the labeled ($\delta^{13}C_{mL}$) and unlabeled ($\delta^{13}C_{mU}$) experiments. The $\delta^{13}C_{mL}$ and $\delta^{13}C_{mU}$ cannot be, however, uniquely measured by the technique used in this study, therefore; the $\Delta\delta^{13}C_m$ is calculated by difference between the measured isotopic composition of a methyl PAH produced during an unlabeled carbonization and the structurally identical methyl PAH produced at 30, 45, and 60 minutes in the ^{13}C labeled carbonization experiments. All enrichments in ^{13}C of alkylated PAH are then reported as the change in isotopic composition of methylated PAH from the unlabeled carbonization experiment. Table 1 gives $\delta^{13}C$ values of individual compounds in Oil C and the following equations were used to calculate the ^{13}C enrichment of the methyl carbons of a given compound:

$$\Delta\delta^{13}C_m\ (‰) = N_m(\delta^{13}C_{mL} - \delta^{13}C_{mU}) = N_{mP}(\delta^{13}C_{mPL} - \delta^{13}C_{mPU})$$

where:

$\Delta\delta^{13}C_m$ = Calculated ^{13}C enrichment due to the labeled methyl carbons.

$\delta^{13}C_{mL}$ = Isotopic composition of the labeled methyl carbons.

$\delta^{13}C_{mU}$ = Isotopic composition of the unlabeled methyl carbons.

$\delta^{13}C_{mPL}$ = Measured isotopic composition of the methyl substituted PAH molecule in the labeled experiment

$\delta^{13}C_{mPU}$ = Measured isotopic composition of the methyl substituted PAH molecule in the unlabeled experiment.

N_{mP} = Number of carbon atoms in the methyl substituted PAH.

N_m = Number of methyl substituents on the PAH.

For example, consider 1-methylnaphthalene at 45 minutes reaction of Oil C,

$N_{mP} = 11$
$N_m = 1$
$\delta^{13}C_{mPL} = 12.7\ ‰$
$\delta^{13}C_{mPU} = -27.4\ ‰$
$\Delta\delta^{13}C_m = 441\ ‰$

The high level of ^{13}C enrichment at the methyl carbon becomes evident with this calculation, as illustrated in Table 1 for $\Delta\delta^{13}C_m$ values for Oil C.

RESULTS AND DISCUSSION

Figure 1 plots the ^{13}C enrichment of specific isomers of monomethyl PAH and pyrene during the course of the reaction for Oil C. All methyl PAH show an increase in isotopic composition with time indicating continual uptake of the ^{13}C-enriched methyl radical. Pyrene, however, does not exhibit any measurable increase in the ^{13}C content. The difference in isotopic composition between methyl substituted and unsubstituted PAH indicates that the ^{13}C-enriched methyl groups do not participate in PAH formation. This behavior was also observed in Filley et al.[4] for Oil A.

A substantial difference in reactivity is evident between methylpyrenes and methyl-substituted naphthalenes and phenanthrenes where the substituted pyrene compounds consistently demonstrate greater uptake of the labeled methyl group. The greater enrichment of methyl- pyrene is a direct indication of higher reactivity of pyrene in alkylation/dealkylation reactions compared to phenanthrene and naphthalene. The methylphenanthrene and methylnaphthalene isomers overlap in Fig. 1.

There are large differences in reactivity between isomers of methylnapthalene, methylphenanthrene and methylpyrene. For example, the α positions of 9- and 1-methylphenanthrene are observed to have greater reactivity with respect to the β substituted 3- and 2-methylphenanthrene. Similarly, the α position of 1-methylnaphthalene is more reactive than the β substituted 2-methylnaphthalene. These results are consistent with calculated free valence indices (FVI) of the positions on the unsubstituted PAH which predict greater reactivity at the α positions toward radical attack[9]. Table 2 shows the FVI for each position on the three PAH. Identical relative reactivities were observed for methylPAH in Oil A (Filley et al.[4]) and Oil B. Figure 2 shows the ^{13}C enrichment of 1-methylnaphthalene and 1-methylpyrene for the three oils,

indicating a higher intrinsic reactivity of pyrene compared to that of naphthalene. High reactivity of pyrenes in methylation/demethylation reactions suggests that pyrenes would also be reactive in radical hydrogenation/dehydrogenation reactions. Eser and Jenkins[10] have discussed the significance of hydrogen transfer reactions in controlling the rate of carbonization and fluidity of the carbonizing medium which are critically important for mesophase development. Liu and Eser[11] reported that high concentrations of pyrenes in coker feedstocks lead to a high degree of mesophase development, which results in the production of needle cokes with high graphitizability.

The consistent reactivity data obtained from three different feedstocks indicates that the reactivity of individual compounds in FCCU slurry oils can control the initial carbonization chemistry. In other words, the molecular composition of a feedstock can dictate the initial reaction pathways during carbonization, and, thus, control the mesophase development[5, 11].

REFERENCES

1. Ettinger, M.; Stock, L.; Gatsis, J. *Energy Fuels* **1994**, 8, 960-971.
2. Voigtment M. F.; Yang K.; Batts, B. D. and Smith, J. W. Fuel **1994**, 12, 1899-1903.
3. Mckinney, D.; Bortiatynski, J.; Hatcher, P. *Energy Fuels* **1993**, 7, 578-581.
4. Filley, T. R.; Filley, R. M.; Eser, S.; Freeman, K.H. *Energy Fuels* **1997**, In Press.
5. Filley, R. M. and Eser, S. *Energy Fuels* **1997**, In Press
6. Ricci, M. P.; Merritt, D. A.; Freeman, K. H.; Hayes, J. M.; *Org. Geochem.* **1994**, 21, 561-571.
7. Merritt, D. A.; Freeman, K. H.; Ricci, M. P.;.Studely, S.; Hayes, J. M.; *Anal. Chem.* **1995**, 67, 2461.
8. Hayes, J. M.; Freeman, K. H.; Popp, B. N.; Hoham, C. H.*Adv. Org. Geochem.* **1990**, 16, 115-1128.
9. Coulson, C. A. and Streitwiesser, A. *Dictionary of π-Electron Calculations*. W.H.Freeman and CO. San Francisco, CA, 1965.
10. Eser, S. and Jenkins, R. G. *Carbon* **1989**, 27, 889-897.
11. Eser, S. and Liu, Y. *ACS Preprints*, Div. Fuel Chem. **38**, 452-459, 1993.

Table 1. Measured $\delta^{13}C$ values and calculated ^{13}C enrichment for the methyl group on selected methyl-substituted PAH formed during the carbonization of FCCU slurry oil C with ^{13}C-labeled4-methyldibenzothiophene.

Compound	30 min		45 min		60 min	
	$\delta^{13}C$ (‰)	Δ	$\delta^{13}C$ (‰)	Δ	$\delta^{13}C$ (‰)	Δ
2-methylnaphthalene (MN)	-22.0	65	-18.5	103	-13.3	161
1-methylnaphthalene (MN)	-3.7	261	12.7	441	27.6	605
3- and 2-methylphenanthrene (MPh)	-20.0	87	-15.0	162	-5.0	312
9- and 1-methylphenanthrene (MPh)	-7.5	260	6.3	467	14.7	593
Pyrene	-25.1	4.8	-24.7	11	-24.4	16
4-methylpyrene (MPy)	16.4	706	39.5	1098	63.1	1499
1-methylpyrene (MPy)	25.1	869	44.8	1204	74.8	1714

Table 2. Calculated Free Valence Indices of different positions on naphthalene, phenanthrene and pyrene (Coulson, et al.)[9]

	FVI
Naphthalene (position 1)	0.452
Naphthalene (position 2)	0.404
Phenanthrene (position 1)	0. 451
Phenanthrene (position 2)	0.402
Phenanthrene (position 3)	0.408
Phenanthrene (position 9)	0.451
Pyrene (position 1)	0.393
Pyrene (position 2)	0.468
Pyrene (position 4)	0.452

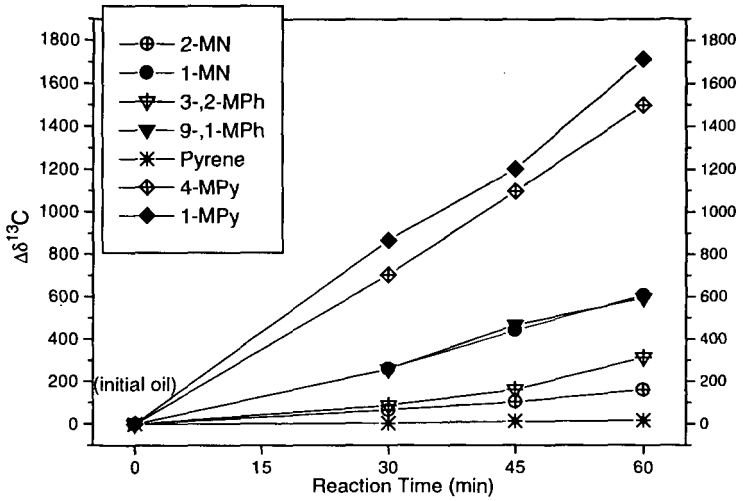

Figure 1. ^{13}C enrichment of the methylsubstituent on selected methylPAH formed during the carbonization of FCCU slurry oil C with ^{13}C-labeled4-methyldibenzothiophene.

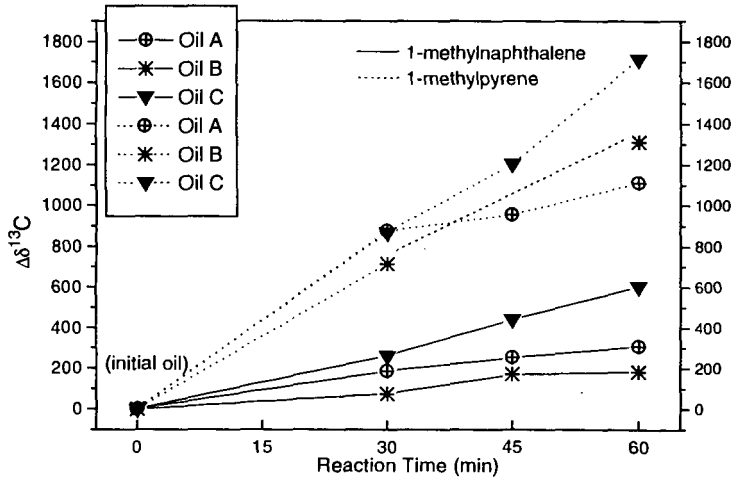

Figure 2. ^{13}C enrichment of the methyl substituent on 1-methylnaphthalene and 1-methylpyrene formed during the carbonization of FCCU slurry Oils A, B, and C with 13C-labeled 4-methyldibenzothiophene.

METALS DETERMINATION BY MICROWAVES DIGESTION AND ICP-AES TECHNIQUE OF UPGRADED LIQUIDS FROM HEAVY PETROLEUM RESIDS

Loredana Caldiero, Monica A. Anelli, Riccardo Nodari, Paolo Pollesel
Eniricerche SpA, Via Maritano 26, 20097 S. Donato Mil. (Milan), Italy

INTRODUCTION

The utilization of heavy petroleum resids and heavy crudes inside the refinery has become one of the most important issues considered and studied by major oil companies. A simple way to utilize heavy fractions with high sulphur and metals' content is blending them with gasoil to produce a fuel to be burned in boilers or furnaces. This route however is becoming more and more difficult, because of increasing stringent environmental regulations. The present work is part of a research project concerning the utilization and the upgrading of heavy oils and of their residues. One of the objectives of the study is to define a process allowing the recovery from heavy resids of lighter and more valuable products which could be reutilized in the standard refinery cycle.
For the upgrading of the residues a continuous pyrolysis process has been considered. Pyrolysis tests, carried out in a rotary kiln system, were aimed to individuate best experimental conditions to maximize the production of liquid products and to increase their quality. The characteristics of the fraction derived from the pyrolysis oils, in fact, must approach the specifications of conventional refinery unit operations, in order to lessen further upgrading treatments. Most of the refinery conversion and upgrading units presents severe limitation on the feedstock heavy metals' content. Therefore the presence of Ni and V in the liquids coming from the pyrolysis process results one of the most important parameters to be investigated to obtain a picture of products' quality.
Laboratory scale runs often produce small quantity of sample to be analyzed and quick responses are requested to direct experimental program. Alternative analytical procedures to traditional ASTM methods are to be defined in order to meet such requirements. Microwaves' digestion to dissolve liquid sample is an advantageous way to perform elemental analysis. The opportunity to work in closed vessels, under elevate pressures and controlled temperatures, avoids time consuming steps, such as incineration and sulphation, and experimental errors due to leaks of volatile compounds or sample contamination. This technique, coupled with an ICP-AES detection, has been emploied to determine Ni and V content in pyrolysis oils as described in this paper.

EXPERIMENTAL

Two different feedstocks were tested: an Italian heavy crude, named "Gela", and the atmospheric residue deriving from the same crude (A.R. ex-Gela). Feedstocks characterization is reported in Table 1. A rotary kiln reactor was chosen to accomplish the pyrolysis step. This system allows to carry on continuous operations and to treat very high viscosity feedstocks. Agglomeration phenomena can be controlled and avoided by a proper optimization of plant operative conditions and by feeding a solid (e.g. sand, coke, dolomite) together with the liquid feed. Liquids feedrate is about 1 kg/h. Temperature, solid residence time and vapor residence time can be set for every run. The coke is dicharged at the reactor exit and collected in a proper vessel. The vapor stream passes through two condensers, where the liquid products are separated, while the gas is filtered, metered ant burned in a flare. Gas samples can be collected after metering and off-line analyzed.
As said above, pyrolysis oil is the most important product. The oil is fractionated according to ASTM D-1160. The oil and the fraction are normally characterized to determine: elemental composition, bromine number (an index of the amount of olefins) for lighter fractions, density for lighter fractions, Conradson Carbon Residue for heavier fractions.
For the most significant runs, i.e. those yielding the largest amount of liquid products, the presence of Ni and V has been investigated. Liquid organic samples (up to 500 mg) have been directly mineralized using a microwaves' digestion system (CEM MDS 2000) which is able to simultaneously process up to twelve PFA closed vessels, under controlled pressure and temperature conditions. The dissolution goes through three subsequent steps involving oxidizing agents as H_2SO_4, HNO_3 and $HClO_4$.
The obtained clear solutions were analyzed by a sequential ICP-AE spectrometer (Perkin-Elmer Plasma 1000) equipped, when necessary, with an ultrasonic nebulizer (Cetac) to reach lower sensitivity, each element at its optimized condition of emission.
All the samples have been added of a proper amount of Sc solution as internal standard. A sample of a NIST standard fuel oil (1634c) was submitted to the same analytical procedure to verify the accuracy of the adopted method.
All the used reagents were of analytical grade of purity.

RESULTS AND DISCUSSION

Pyrolysis tests

Pyrolysis results showed that maximum liquids yield is obtained at a temperature of 500°C. Vapor residence time (τ_{gas}) did not show pronounced effects on products distribution. However runs with higher residence time produced lighter, and therefore more valuable liquids. Table 2 shows products yield and fractions' distribution for two runs with A.R. ex-Gela and for the best run with Gela crude.
Pyrolysis oil is the main product in every run, yielding more than 50 wt. %. Gela test gives a higher liquid yield, being a less heavy feedstock compared to the atmospheric residue. 170-350°C fraction is the most important in all the pyrolysis oils obtained. Even if only a few runs are reported here, some results can be pointed out. The positive effect of an increased τ_{gas} is highlighted by the comparison between fraction distributions for run RATM10 and run RATM18. The latest (τ_{gas}= 53 s) shows a distribution clearly shifted towards lighter fractions, concerning the run with shorter τ_{gas} (21 s). Fractions' characterization for the three runs are listed in Table 3. More details about overall mass balances and products analyses are reported elsewhere /1/.

Analytical results

Ni and V were determined on unfractionated pyrolysis oils and on the related distillation fractions. The adopted procedure utilizes the idea of subsequential oxidations performed by stronger and stronger agents. The optimization proceeded by varying microwaves' power, expressed as percentage of full scale, run time, reaction pressure and temperature.
All the samples were pretreated at the same way:
Up to 500 mg of sample was put in a PFA vessel and added with 2-3 ml of H_2SO_4. The vessel, opened, was then subjected to the following microwaves' steps:

STEP	1	2
Power (%)	20	0
Run Time(min)	20	20
P (psi)	-	-
T (°C)	-	room

Vessels: up to twelve

The H_2SO_4 (boiling point 330°C) is a strong oxidizing agent when hot. In this mild step it is preferred working with open vessel to reach higher temperature regarding those achievable under control by the optical fiber. After the treatment the sample looks like a "char".
The sample is then added of up to 10 ml HNO_3 and the closed vessel is put in the microwaves' system to undergo the following steps:

STEP	1	2	3	4	5
Power (%)	40	60	70	90	0
Run Time (min)	15	15	15	20	0
P (psi)	80	120	160	200	20
T (°C)	80	120	160	185	room

Vessel: up to twelve

To the cool solutions 1-2 ml $HClO_4$ are added. The final digestion steps are following described:

STEP	1	2	3	4	5
Power (%)	50	60	75	90	0
Run Time (min)	10	15	15	30	0
P (psi)	50	100	120	200	20
T (°C)	120	140	160	185	room

Vessel: up to twelve

The clear yellow solutions containing all metal perchlorates, very soluble in water, were then prepared to be analyzed by ICP-AES.
The described procedure, what's more it is based on simple analytical concepts of gradual oxidation, allows in a very short time (less than three hours) to process up to twelve samples having organic matrix, employing quite small amounts of reagents, and assuring prevention of leaks or external pollution.
The solutions were transferred into calibrated flasks, in which an aqueous solution of Sc was added. The Sc as internal standard is suggested by the instrument supplier to use the Myer-Tracy system /2/ which allows a more correct analyte determination as it reduces the short term noise and signal fluctuation due to the sample nebulization process. Ni and V were detected at λ=

231.604 nm and λ=309.311 nm respectively. The instrument calibration was performed utilizing three standard solutions and a blank containing all the same reagents present into the unknown solutions.
Results obtained on unfractionated oils and on respective distillation cuts are summarized in Table 4, together with mass balance to check the method's precision.
As expected metals concentrate in the heaviest cut. The small amount of Ni and V detected in the 170-350°C fractions seems quite unusual, with respect to conventional petroleum products, where metals are normally absent in lighter cuts. Moreover in 350-500°C fractions, metals are in fact almost absent. However repeated tests have confirmed present results. This particular aspect will be further investigated more thoroughly.
Mass balance data confirm the initial results and suggest the reliability of this method. The good comparison between the experimental data obtained applying the described procedure on a standard fuel oil and the certified values (Table 5) also guarantees the accuracy of the technique.

CONCLUSIONS

Upgradated liquid products have been obtained from heavy petroleum resids through a pyrolysis process. The presence of Ni and V in these products has been investigated using a particular technique of sample preparation and treatment. The method allows to treat small quantity of sample, prevents the occurrence of leaks oor external contamination and can process up to twelve samples in less than three hours. Results have been compared and validated by process mass balance and by the succesful application of the technique to a standard fuel oil.

REFERENCES

/1/ A. Carugati, L. De Vita, G. Pederzani, P. Pollesel, Proc. of "Gasification Technology in Practice", February 26-27, 1997, Milan (Italy).
/2/ Tiggelman, J.J., Oukes F.J. et al., Spectrochim. Acta, Part B, 1990, 45B(8), 927-32

Table 1. Feedstocks characterization.

	Gela crude	A.R. ex-Gela
Elemental analysis (wt. %)		
Carbon	81.11	81.49
Hydrogen	10.7	9.91
Nitrogen	0.41	0.56
Sulphur	7.42	7.97
Metals (ppmw)		
Nickel	90	127
Vanadium	125	186
Conradson Carbon R. (wt. %)	12.86	18.13
Density at 15°C (g/ml)	0.9977	1.0892
Viscosity at 100°C (c.St)	115	2,177

Table 2. Pyrolysis products distribution.

Run	T	τ_{gas}	τ_{solids}	Products (wt. %)			Liquid fractions (wt. %, oil basis)			
	°C	s	min	gas	oil	coke	ibp-170	170-350	350-500	500°C+
RATM10	500	21	30	39.3	51.2	9.5	6.67	45.40	31.50	16.33
RATM18	500	53	30	37.5	50.7	11.8	16.91	60.98	16.08	6.02
GELA3	500	50	30	30.5	58.4	11.1	16.53	49.93	23.89	9.65

Table 3. Characterization of the fractionated pyrolysis oils.

	C	H	S	N*	n.Br**	CCR**	ρ**
	(wt. %)					(wt.%)	(g/ml)
RATM10 ibp-170	82.51	13.37	2.51	43	93.4		0.7683
RATM10 170-350	83.24	12.56	3.82	555	43.7		0.8497
RATM10 350-500	79.80	9.94	6.83	0.19		0.75	
RATM10 500°C+	81.46	8.51	8.46	0.39		23.19	
RATM18 ibp-170	83.25	13.32	1.55	56	85.7		0.7566
RATM18 170-350	83.22	12.34	4.04	912	48.3		0.8410
RATM18 350-500	82.43	9.92	7.29	0.23		1.11	
RATM18 500°C+	81.45	7.98	8.92	0.50		29.12	
GELA3 ibp-170	83.64	13.19	2.23	48	98.4		0.7758
GELA3 170-350	83.34	11.91	4.24	452	43.1		0.8799
GELA3 350-500	80.63	9.83	6.45	0.21		0.83	
GELA3 500°C+	80.67	7.72	8.99	0.42		31.58	

* = Nitrogen amount is expressed in ppmw for ibp-170 and 170-350 cuts; while it is wt. % for 350-500 and 500°C+ cuts.

** = Bromine number and density have been determined only for the lighter fractions. CCR has been determined only for the heavier fractions.

Table 4. Ni and V samples' content (ppmw) and mass balance.

Run	Unfractionated oil		Distillation cuts						Sum of fractions	
			170-350		350-500		500°C+			
	Ni	V	*Ni*	V	*Ni*	V	*Ni*	V	*Ni*	V
RATM10	8.4	9.0	1.6	1.3	0.9	<0.5	46.1	52.6	8.5	9.2
RATM18	3.2	2.9	1.7	2.0	<0.5	<0.5	42.3	46.4	3.6	4.0
GELA3	4.9	3.9	2.3	0.6	2.2	<0.5	24.9	28.8	4.1	3.1

Table 5. Ni and V results (ppmw) on NIST standard: comparison between experimental and certified values (the expanded uncertainties are level of confidence of 95%).

	NIST 1634C Standard Fuel Oil
Ni certified	7.5 ± 0.2
Ni experimental	7.2 ± 0.4
V certified	28.2 ± 0.4
V experimental	28.3 ± 0.3

RADIOISOTOPE STUDY INTO Co AND Ni CONTAINING CATALYSTS FOR PETROLEUM RESIDUA HYDROTREATING

Victor M. Kogan[a], Natalia M. Parfenova[b]

[a]*N.D.Zelinsky Institute of Organic Chemistry, Russian Academy of Sciences, 47 Leninsky prospect, Moscow 117913, Russian Federation;*

[b]*Institute of Chemistry, Turkmenian Academy of Sciences, 92 Pogranichnicov st, Ashgabat 744012, Turkmenistan.*

A comparative radioisotope study into alumina- and silica supported Co, Ni and Co+Ni catalysts has been carried out. Catalysts were characterized by physical and chemical methods and tested during hydrotreating (HTR) of oil residua of West-Sibirian petroleum. Some dependencies among catalyst composition, carrier support, the number, type and productivity of active sites, and catalyst functioning under oil residua HTR have been found. The study has permitted us to put forward some criteria to evaluate the results of radioisotope testing with the aim of designing a catalyst composition optimum for a definite refining process. Some cheap catalysts-adsorbents for preliminary treating of heavy crudes, before they are applied to the main oil refining processes have been designed.

1. INTRODUCTION

Involving heavy residual oils into refining processing makes it of major importance to have effective catalysts for oil HTR. Some major concepts of HTR reactions and architecture of the supported catalysts have been already formulated [1 - 22]. Nevertheless, studies into supported catalyst composition and principles of their functioning are still very urgent to which fact testifies a great number of articles and reviews [10, 11, 23 - 29] which are mainly focused on the issue of catalyst composition and not so often on reaction mechanisms. Radioisotope technique offers us extra opportunities to obtain unique information on active sites number and their functioning and heterocompound transformation mechanisms. [30 - 36].

In this paper the comparison of the results of catalyst radioisotope testing during model reaction of thiophene HDS with the data of residual oil HTR on the same catalysts is being undertaken. It aims at adequate evaluating of both methods potentials to design the best catalyst composition for an actual HTR process.

2. EXPERIMENTAL

2.1. Catalyst preparation, characterization and pretreatment

More than 70 Ni- and Co-containing catalysts were synthesized and studied. Catalyst samples were prepared by wet impregnation of γ-Al_2O_3 (specific surface - 212 m^2/g, pore volume - 0.8 cm^3/g, pore average D - 124 Å) and of SiO_2 (specific surface - 363 m^2/g, pore volume - 0.96 cm^3/g, pore average D - 98 Å). Impregnation procedure was carried out (i) using water solutions of Ni or Co nitrates for preparing Ni or Co catalysts, or (ii) using join solution of Co and Ni nitrates - for Ni+Co catalyst samples preparing. After impregnation the catalysts were air dried for 24 h at room temperature and 2 h at 110°C. Metal surface amount in the samples varied in the range of 1 - 25 %.

All the carriers and catalysts were studied by physico-chemical methods. Pore structure was determined by Hg porometry technique using *Cultronix* automatic porometer. Metal reduction degree was determined by volumetric technique. Metal concentration in the catalysts was measured by atomic absorption technique.

Two forms of the catalysts were used - reduced and sulfidized. Sample reduction was carried out in the flow of purified H_2 for 10 h at 400°C. Sulfidation of preliminary reduced catalysts was made by elemental sulfur in hydrogen atmosphere (3 MPa, 380°C, 1 h).

2.2. Residual oil hydrotreating technique and product characterization

Residual oils of West-Sibirian petroleum contained: asphaltenes - 4.3 % wt, sulfur - 2.3 % wt, V - 40 g/t, Ni - 60 g/t. Residual oil HTR was carried out in a 250 cm^3 stainless steel autoclave (5 MPa H_2 pressure, 380°C, 5 h). Sulfur amount in crudes was determined analytically. Derivatographic measurements of coke deposits on the catalyst were made.

2.3. The technique of HDS experiments with radiochromatographic analysis of the products.

2.3.1. *Catalyst sulfidation* was carried out in a pulse microcatalytic installation. The microreactor in the form of U-tube made of pyrex was loaded with 100 mg of the catalyst and linked with the gas-liquid (GL) chromatograph. The rest of the reactor volume was filled with quartz. All catalysts were preliminary subjected to He flow at 200°C for 2 h, then by H_2 flow, 400°C, 4 h. After that they were sulfidized. As sulfidizing agent either 5 % H_2S/H_2, in which H_2S was labeled by ^{35}S isotope,

or thiophene-^{35}S was used. H_2S/H_2 sulfidation lasted for 1 h at 450°C. Further on the catalyst was again treated by He at the same temperature for 30 min. to get rid of adsorbed H_2S.

Sulfidation by thiophene-^{35}S was made by 3 μl thiophene pulsing into the reactor at 360°C with further chromatographic analysis of the products. After H_2S curve became constant thiophene-^{35}S pulsing was stopped. After sample sulfidation was over, reactor temperature stabilized at 360°C. Then the catalyst either was taken out of the reactor for sulfide sulfur amount measurement or was tested in the reaction of thiophene HDS.

2.3.2. *The technique of HDS experiments with radiochromatographic analysis of the products and mathematical treatment of experiment results.* After sulfidation procedure catalyst samples labeled by ^{35}S were tested in the thiophene HDS reaction. Unlabeled thiophene was injected into the reactor by pulses, 1 μl each. To measure reaction product radioactivity a flow proportional counter installed in the outlet of the chromatograph was used. Based on the results obtained some curves of H_2S molar radioactivity (MR) dependencies on H_2S amount (cm^3) are built equivalent to the dependencies on reacted thiophene amounts. Mathematical treatment of the experimental curves allows us to approximate the dependencies we obtained by exponential equations and to calculate the amount of mobile sulfur on each type of active site and productivities of these sites [35].

3. RESULTS AND DISCUSSION

3.1. Radioisotope testing

Preliminary experiments with various amounts of active metal on the catalyst have shown that catalytic activity curves of the samples under study pass through a maximum, depending on an active component amount. The maximum area for all the contacts under study is in the range of 7.0 - 7.6 %. So, those catalyst samples that contain the given amount of active metal have been studied in detail. The results are shown in Tables 1 and 2.

Measurements of radioactivity of thiophene hydrogenolysis products on all the catalysts containing sulfide sulfur labeled by ^{35}S show that radioactivity is present only in H_2S formed. Thiophene that leaves the reactor does not contain radioactivity, which points to the absence of isotope exchange between thiophene sulfur and catalyst sulfide sulfur. In the intervals of thiophene pulses into the reactor or under special experiments any noticeable amount of H_2S formed is not found, *i.e.* any marked sulfidized catalyst reduction does not occur. H_2S is formed only as a product of thiophene hydrogenolysis.

Table 2 gives equations for the curves of dependencies of H_2S molar radioactivity (MR) on the amount of H_2S formed under thiophene HDS on the catalysts sulfidized by radioactive sulfur. One can see that these equations are monoexponential, *i.e.* Co or Ni catalysts or Co+Ni catalysts have one type of H_2S formation site while Co(Ni) promoted Mo catalysts have two types of sites differing on the mobility of sulfur, *i.e.* productivity [35].

Figure 1 shows that treating the reduced catalyst by H_2S/H_2 always results in much deeper sulfidation as compared to thiophene. Share of mobile sulfur in samples sulfidized by H_2S/H_2 ranges within 11 - 50 % and in Ni or Co+Ni catalysts it is higher than in Co ones. It is true both for alumina- and silica supported catalysts and may be due either to high dispersion of Ni-sulfide particles as compared to Co-sulfide ones or to probable CoS_2 phase formation. It is also essential that on alumina supported catalysts, sulfidized by H_2S/H_2, mobile sulfur share is larger than on analogous catalysts supported on silica. It might also be accounted for by higher dispersion of sulfide particles supported on alumina as compared to that of particles supported on silica.

Unlike in catalysts sulfidized by H_2S/H_2, in catalysts sulfidized by thiophene sulfidation does not reach maximum possible values and all sulfide sulfur formed under sulfidation by thiophene is mobile. Major portion of mobile sulfur is on Co/SiO_2 sulfidized by thiophene (sample 2a in Table 1) - 2.42 % and the least (0.63 %) - on the same catalyst sulfidized by H_2S/H_2 (2b). In the first case mobile sulfur equals 100 % of all catalyst sulfide sulfur and in the second - only 11 %. Productivity of Co/SiO_2 catalyst active sites is also much dependent on a sulfidation procedure - under H_2S/H_2 sulfidation it is twice as high as under thiophene. It can be also noted here that this difference is common to other catalysts. In some cases it is noticeably large while in others not (for instance, for Ni/SiO_2 it is not higher than 10 %). We may suppose that under full sulfidation the formation of a substantial amount of immobile sulfur encourages active site formation that have more mobile SH groups as compared to a phase where all sulfur is mobile.If compare Co/SiO_2 and Co/Al_2O_3 catalysts, sulfidized in the same way, one can see that productivities (P) of active sites of these are close. It can be caused by an insignificant effect of carrier nature on reactivity of active sites and by an essential effect of a carrier on the number of the sites.

An effect of active phase metal nature on catalyst active site productivity is clearly seen in the sequence Co - (Co+Ni) - Ni. In all the catalysts supported by one and the same carrier and sulfidized in the same way the productivity grows in the sequence Co ≤ (Co+Ni) ≤ Ni. Thus, SH groups of Ni-sulfide particles demonstrate higher reactivity in H_2S formation under thiophene HDS conditions than analogous SH groups connected with Co. A possible explanation of these dependencies might be searched within Bond Energy Model, recently developed by Topsøe *et al* [37].

The results of radioisotope testing permit us to single out three catalysts with the best characteristics - Co/SiO_2 (sample 2a), $(Co+Ni)/Al_2O_3$ (5b) and Ni/Al_2O_3 (3b). Sample 2a is characterized by the highest amount of mobile sulfur, though its active site productivity is the lowest and it demonstrates no high activity in thiophene HDS. Sample 5b demonstrates the highest thiophene conversion, its mobile sulfur amount is actually the same as in sample 2a, and *P* is considerably higher than in most of catalysts under study. Finally, sample 3b has the highest *P*, highest thiophene conversion and relatively small amount of mobile sulfur. To evaluate the effect of the given parameters on the catalyst functioning under real conditions we have compared them with the data obtained in the course of hydroconversion of residual oil.

3.2. Hydrotreating of residual oil

In the course of the experiments it has been found that, the same as in the above described experiments, most effective have proved catalysts containing 7.5 % metal. Catalysts with 3.4 % metal loading were ineffective. Catalytic activity of samples with metal loading 10 % and higher did not exceed that of the catalysts with 7.5 % metal content.

The data about hydrotreating of residual oil is given in Table 3. First it should be stressed that all the catalysts show a rather high degree of selectivity towards residual oil containing metals (Ni, V) that are poisons for cracking catalysts. The catalysts demonstrate different degree of activity towards the desulfurization reaction, depending on the nature of an active metal and support (Fig. 2). The most active is Co/SiO_2 in reduced form (sample 2a, Table 3) - residua desulfurization degree is 55.7 %. Somewhat less active are reduced catalysts Co/Al_2O_3 (1a) and $(Co+Ni)/SiO_2$ (6a) - 26 % and 27 % correspondingly. Ni reduced catalysts on alumina (3a) and silica (4a) show much less desulfurization activity - 18.0 % and 16.5 % correspondingly. Reduced Co/SiO_2 shows the highest activity in relation to deasphaltization and the lowest towards coke formation. In this catalyst on the silica surface metallic Co of fine dispersion with crystallite size 25 Å has been found. No formation of surface compounds with support is observed. The catalyst has a high specific surface 307 m^2/g pore volume 0.78 cm^3/g, pore average D 46 Å. Co reduction degree is 97 %. If compare pore structure of the support and catalyst one can see that Co loading does not much change the value of specific surface and pore size. It is possible that in the course of the reaction with sulfur containing crudes Co-sulfide particles formation takes place and they are active in hydrogenation (HYD) reactions. Catalyzing residua asphaltenes HYD they practically completely adsorb metals (Ni and V), which leads to a high degree of residua demetallization. Co sulfides as well as pure Co on silica do not catalyze HYD process of hydrocarbons, which is proved by a low coke deposition on these catalysts.

Co/Al_2O_3 in its reduced form (1a) has a sharp difference from Co/SiO_2: desulfurization degree is twice as low and asphaltene disintegration degree is about 50 %. Demetallization degree is lower too. In all probability, incorporation of some part of Co particles in the Al_2O_3 carrier material decreases the ability of Co/Al_2O_3 to interact with the sulfur of residua heterocompounds.

Ni/SiO_2 reduced catalyst (4a) differs with Co one on its catalytic action. Its desulfurization degree is more than three times lower but it is active in asphaltene HYD, demetallization and coke formation. These data testifies to the fact that metallic Ni on silica weakly interacts with the sulfur of sulfurorganic compounds from residual oil and more actively in HYD and deHYD reactions. Reduced Ni/Al_2O_3 (3a) is more active than Ni/SiO_2 in reactions of C-C bond break and coke formation and less active in asphaltene HYD.

Sulfidized forms of Co and Ni catalysts are essentially different from reduced forms of this catalysts on their catalytic activity, which supposes other nature of their interaction with oil residua components. All the sulfide catalysts have proved to be less active in deasphaltization but more active in coke formation (Tab. 3, Fig. 3). Sulfidized Co/SiO_2 (2b) shows the least degree of desulfurization - 13.6 % and highest degree of demetallization among the sulfide catalysts. Obviously, Co sulfide particles in 2a are not so active in desulfurization than reduced Co particles of sample 2b. Sulfidized Ni/Al_2O_3 catalyst (3b) shows rather low activity in oil residua desulfurization, the same as in demetallization and tends to coke formation. A high activity in oil residua desulfurization has been shown by sulfidized $(Co+Ni)/Al_2O_3$ catalyst (5b) - 46 % and at the same time its degree of demetallization is the lowest - 61 %. Its coke deposition is 4.6 %.

3.3. Comparative study of radioisotope testing and residual oil hydrotreating data

While comparing the data of radioisotope testing with the results of residual oil HTR one can see a correlation between residual oil desulfurization degree and the amount of mobile sulfur on the catalyst (Fig. 4). Previously we observed a linear dependency between thiophene conversion and the amount of mobile sulfur in CoMo catalysts [33, 34]. However, as it was found later [35], this dependency was true not in all cases but only for the catalysts active sites of which are characterized by close values of productivity. In Table 1 one can see no correlation between thiophene conversion and the amount of mobile sulfur due to the fact that active site *Ps* of these catalysts differ from each other as much as two - threefold. In case of residual oil, however, such correlation is seen. One can suppose that a large number of contained in crudes and subjected to desulfurization sulfurorganic compounds which possess different degrees of stability in destruction processes as if levels the

values of P of different catalysts.

Hence, it seems we could conclude that such value as productivity is not essential when we deal with processes based on real crudes. But actually it not so at all. It was rather surprising to establish another linear dependency - between productivity of H_2S formation active sites and coke formation on the catalyst - a secondary process in relation to HDS and H_2S formation (Fig. 5). To some extent this dependency can be explained by carrier acidity on coke formation and hydrodesulfurization. The interdependency between carrier acidity and coke formation is commonly known and the dependency between catalytic activity and carrier acidity is marked by Welters *et al.* [38, 39]. Tables 1 and 3 show that the samples of analogous composition and sulfidized in the same way but supported on different carriers differ on the amount of coke deposition and site productivity - for Al_2O_3-supported catalysts these values are higher than for their SiO_2-supported analogs. But this fact can only partially serve as an explanation to the marked dependency. For instance, by acidity one cannot explain higher tendency of Ni-containing catalysts towards coke formation. It seems probable that the higher site productivity the more hydrocarbon fragments are formed in the course of destruction of sulfurorganic molecules and the higher coke formation is.

This supposition is confirmed when we compare the results of residual oil HTR on the above described catalysts non-containing Mo with the results of the same procedure on the commercial Ni-Mo/Al_2O_3 sulfidized catalyst (see Table 3, sample 7). This catalyst has a high desulfurization ability, being inferior only to catalysts 2a and 5b, but it displays rather low demetallization activity and the strongest tendency towards coke formation. The results of radioisotope testing of Ni-Mo/Al_2O_3 were submitted and discussed in [35]. In this paper we present radioisotope testing data only for one, mentioned above, commercial catalyst (the last lines of Tables 1 and 2, sample 7) for comparison with data obtained for non-containing Mo catalysts. Sample 7 is characterized by the presence of two types of active sites, "rapid" and "slow", Ps of which are 20.1×10^{-2} and 5×10^{-2} correspondingly and the number of the 'rapid" sites is 25 % of the total number of the both types of the sites. The amount of mobile sulfur is 41 % of the total sulfide sulfur in catalyst 7. On this catalyst under the same experimental conditions as for the other catalysts thiophene HDS conversion is 59 % *i.e.* much higher than on the catalysts without Mo.

We believe that on the Mo catalyst promoted by Ni or Co the "rapid" sites are related to Mo and the "slow" ones - to Ni or Co. It was shown [33 - 35] that the unpromoted Mo/Al_2O_3 catalyst has one type of the sites of low P ($\approx 5\times10^{-2}$), low catalytic activity in the thiophene HDS (conversion $\approx$ 12 %) and the share of mobile sulfur is about 20 % of the total sulfur amount on the catalyst. Introducing promoter (Ni or Co) increases P of active sites related to Mo, though some part of these are blocked by Ni(Co)-sulfide particles. The total of the active sites on the promoted catalyst grows as compared to the unpromoted one because of an increase in "slow" sites. Evidently, the role of the "rapid" sites in catalyst functioning is dual: on the one hand, the sites increase catalytic activity, on the other - they encourage coke deposition of the catalyst. It is particularly important when processing heavy crudes. It is this dual role of "rapid" sites that we observe during residual hydrotreating on sample 7: the total mobile sulfur is high (actually is the same as in sample 5b), which leads to a high desulfurization activity, and a high P of some part of active sites results in strong coke formation. Thus, there seems to be some ground to state that when selecting most efficient catalysts for residual oil preliminary hydrotreating one should consider as preferable the systems with great amount of mobile sulfur. *i.e.* relatively high number of active sites and low productivity of these.

The study discussed in this paper has permitted us to put forward two catalysts - 7.4 % Co/SiO_2 in its reduced form (sample 2a) and (3.4 % Co + 4.1 % Ni)/Al_2O_3 in its sulfide form (sample 5b) as catalysts-adsorbents for the first stage of hydrotreating of heavy crudes. An important advantage of these catalysts is their relative cheapness due to the absence of expensive Mo in them.

CONCLUSIONS

i. The present investigation gives us ground to state that when selecting most efficient catalysts for residual oil preliminary hydrotreating one should consider as preferable the systems with great amount of mobile sulfur. i.e. relatively high number of active sites and low productivity of these.

ii. The study has permitted us to put forward two catalysts - (7.4 % Co)/SiO_2 in its reduced form and (3.4 % Co + 4.1 % Ni)/Al_2O_3 in its sulfide form as catalysts-adsorbents for the first stage of hydrotreating of heavy crudes. An important advantage of these catalysts is their relative cheapness due to the absence of expensive Mo in them.

REFERENCES

1. J.M.J.G. Lipsh and G.C.A. Schuit, J. Catal., 15 (1969) 163, 174, 179.
2. S.C. Schuman and H. Shalit, Catal. Rev., 4 (1970) 245.
3. R.J.H. Voorhoeve and J.C.M. Stuiver, J.Catal., 23 (1971) 243.
4. G. Hagenbach, Ph. Courty and B. Delmon, J.Catal., 23 (1971) 295.
5. G. Hagenbach, Ph. Courty and B. Delmon, J.Catal., 31 (1973) 264.
6. G. Hagenbach, P. Menguy and B. Delmon, Bull. Soc. Chim. Belg., 83 (1974) 1.
7. C.H. Amberg, Less-Common Met., 36 (1974) 339.
8. P. Grange and B. Delmon, Less-Common Met. 36 (1974) 353.
9. T. Ohtsuka, Catal. Rev., 16 (1977) 291.
10. F.E. Massoth, Adv. Catal., 27 (1978) 265.
11. P. Ratnasamy and S. Sivasanker, Catal. Rev. - Sci. Eng., 22 (1980) 401.
12. H. Topsøe, B.S. Clausen, R. Candia, C. Wivel and S. Morup, Bull. Soc. Chim. Belg., 90 (1981) 1189.
13. H. Topsøe, B.S. Clausen, R. Candia, C. Wivel and S. Morup, J. Catal, 68 (1981) 433, 453.
14. N.-Y. Topsøe and H. Topsøe, Bull. Soc. Chim. Belg., 90 (1981) 1311.
15. H. Topsøe, R. Candia, N.-Y. Topsøe and B.S. Clausen, Bull. Soc. Chim. Belg., 93 (1984) 783.
16. S. Kasztelan, H. Toulhoat, J. Grimblot and J.P. Bonnelle, Appl. Catal., 13 (1984) 127.
17. B. Delmon, Surface and Interface Anal., 9 (1986) 195.
18. S. Kasztelan, L. Jalowiecki, A. Wambeke, J. Grimblot and J.P. Bonnelle, Bull. Soc. Chim. Belg., 96 (1987) 1003.
19. N.-Y. Topsøe, H. Topsøe and F.E. Massoth, J.Catal., 119 (1989)119, 252.
20. L. Viver, P. D'Araujo, S. Kasztelan and G. Perot, J. Mol. Catal., 67 (1991) 267.
21. L. Viver, P. D'Araujo, S. Kasztelan and G. Perot, Bull. Soc. Chim. Belg., 100 (1991) 807.
22. U.S. Oskan, L Zhang, S. Ni and E. Moctezuma, J.Catal., 148 (1994) 181.
23. M. Zdrazil, Appl. Catal., 4 (1982) 107.
24. M.L. Vrinat, Appl. Catal., 6 (1983) 137.
25. R. Prins, V.H.J. de Beer and G.A. Somorjai, Catal. Rev. - Sci. Eng., 31 (1989) 1.
26. B. Delmon, Catal. Lett., 22 (1993) 1.
27. B. Delmon, Bull. Soc. Chim. Belg., 104 (1995) 173
28. A.N. Startsev, Catal. Rev. - Sci. Eng., 37 (1995) 353.
29. H. Topsøe, B.S. Clausen and F.E. Massoth, Hydrotreating Catalysis - Science and Technology, Edited by J.R. Anderson and M. Boudart, Vol. 11, ISBN 3-540-60380-8 Springer-Verlag Berlin Heidelberg, 1996.
30. G.V. Isagulyants, A.A. Greish and V.M. Kogan, Kinetics and Catalysis, Engl. tr., 28 (1987) 220.
31. G.V. Isagulyants, A.A. Greish, V.M. Kogan, G.M.V'unova. G.V.Antoshin, Kinetics and Catalysis, Engl. tr., 28 (1987) 550.
32. G.V. Isagulyants, A.A. Greish and V.M. Kogan, Kinetics and Catalysis, Engl. tr., 28 (1987) 555..
33. G.V. Isagulyants, A.A. Greish and V.M. Kogan, in: "Proc. 9-th Int.Congress on Catalysis", (Calgary, 1988), eds. M.J. Philips and M. Ternan, 1988, Vol. 1, P. 35.
34. V.M. Kogan , A.A. Greish and G.V. Isagulyants, Catal. Letters, 6 (1990) 157.
35. V.M. Kogan, Nguen Thi Dung and V.I. Yakerson, Bull. Soc. Chim. Belg. 104 (1995) 303.
36. V.M. Kogan , A.A. Greish and G.V. Isagulyants, in "Proc. 2-th European Congress on Catalysis", Maastricht, 3-8 September 1995, P.23.
37. H. Topsøe, B.S. Clausen, N.-Y. Topsøe, J.K. Nørskov, C.V. Ovesen and C.J.H. Jacobsen, Bull. Soc. Chim. Belg., 104 (1995) 283.
38. W.J.J. Welters, G. Vorbeck, H.W. Zandbergen, J.W. de Haan, V.H.J. de Beer and R.A. van Santen, J.Catal., 150 (1994) 155.
39. W.J.J. Welters, V.H.J. de Beer and R.A. van Santen, Appl. Catal., 119 (1994) 253.

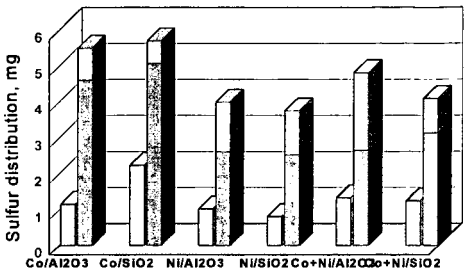

Figure 1. Sulfur distribution *vs.* catalyst composition and pretreatment procedure. Left bars - samples sulfidized by thiophene; right bars - by H_2S/H_2. Light parts of bars - mobile sulfur; dark ones - immobile sulfur (see experimental conditions in Tables 1 or 2).

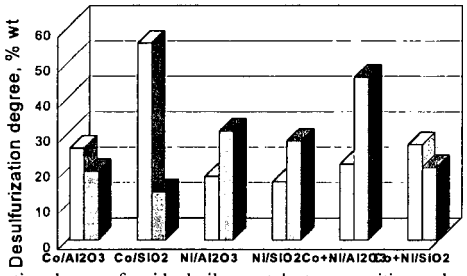

Figure 2. Desulfurization degree of residual oil *vs.* catalyst composition and pretreatment procedure. Left bars - reduced catalysts; right ones - sulfidized catalysts.

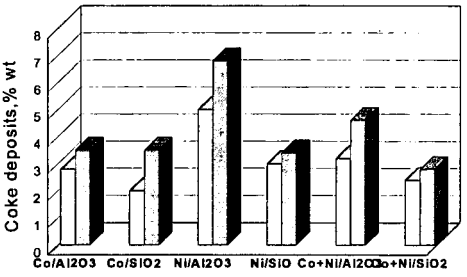

Figure 3. Coke deposition on the catalyst *vs.* composition and pretreatment procedure. Left bars - reduced catalysts; right ones - sulfidized catalysts.

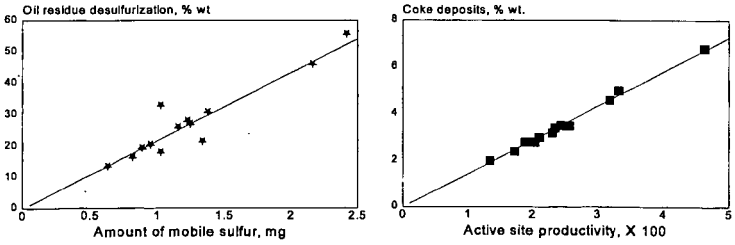

Figure 4. Oil residua desulfurization degree *vs.* amount of mobile sulfur on the catalysts under study.

Figure 5. Coke deposition on the catalyst samples *vs.* active site productivity.

Table 1: Results of radioisotope testing of catalysts in the reaction of thiophene HDS (100 mg sample loading, 360°C, H_2 flow, pulses of thiophene-1-l)

No. smp	Catalyst composition	Pretreatment agent	S_{total} % wt	S_{mob} % wt	S_m/S_t %	*, % mol	P** TM 10^2
1a	(7.0%Co)/Al_2O_3	thiophene	1.16	1.16	100	5.40	1.89
1b	(7.0%Co)/Al_2O_3	H_2S/H_2	5.50	0.89	16.2	5.34	2.43
2a	(7.4%Co)/SiO_2	thiophene	2.42	2.42	100	8.00	1.34
2b	(7.4%Co)/SiO_2	H_2S/H_2	5.70	0.63	11.1	4.00	2.56
3a	(7.6%Ni)/Al_2O_3	thiophene	1.03	1.03	100	8.43	3.33
3b	(7.6%Ni)/Al_2O_3	H_2S/H_2	4.00	1.38	34.5	15.70	4.63
4a	(7.3%Ni)/SiO_2	thiophene	0.82	0.82	100	4.25	2.10
4b	(7.3%Ni)/SiO_2	H_2S/H_2	3.76	1.23	32.7	7.25	2.34
5a	(3.4%Co+4.1%Ni)/Al_2O_3	thiophene	1.34	1.34	100	7.62	2.30
5b	(3.4%Co+4.1%Ni)/Al_2O_3	H_2S/H_2	4.82	2.16	45.0	17.00	3.19
6a	(3.5%Co+3.5%Ni)/SiO_2	thiophene	1.25	1.25	100	5.35	1.73
6b	(3.5%Co+3.5%Ni)/SiO_2	H_2S/H_2	4.10	0.95	23.2	4.15	2.03
7***	Ni-Mo/Al_2O_3	H_2S/H_2	6.08	2.49	41.0	59.00	20.1 5.4

*) γ - thiophene conversion; **) P - active site productivity; ***) commercial catalyst

Table 2: Change of H_2S molar radioactivity (α) in the course of thiophene HDS on sulfide-^{35}S catalysts (100 mg sample loading, 360°C, H_2 flow, pulses of thiophene-l-1)

No smp	Catalyst	H_2S MR	No smp	Catalyst	H_2S MR
1a	Co/Al_2O_3	= 100 exp(-1.23x)	4a	Ni/SiO_2	= 100 exp(-1.74x)
1b	Co/Al_2O_3	= 100 exp(-1.60x)	4b	Ni/SiO_2	= 100 exp(-1.16x)
2a	Co/SiO_2	= 100 exp(-0.59x)	5a	(Co+Ni)/Al_2O_3	= 100 exp(-1.07x)
2b	Co/SiO_2	= 100 exp(-2.26x)	5b	(Co+Ni)/Al_2O_3	= 100 exp(-0.66x)
3a	Ni/Al_2O_3	= 100 exp(-1.39x)	6a	(Co+Ni)/SiO_2	= 100 exp(-1.14x)
3b	Ni/Al_2O_3	= 100 exp(-1.04x)	6b	(Co+Ni)/SiO_2	= 100 exp(-1.50x)
7	NiMo/Al_2O_3	= 52.08 exp(-1.20x) + 47.92 exp(-0.32x)			

Table 3: Results of hydrotreating residual oil of West-Sibirian petroleum (initial residual oil contained: asphaltenes - 4.3 %, S - 2.3 %, V - 40g/ton, Ni - 20 g/ton).

No smp	Catalyst composition	Pre-treatment*	Desulfur. degree, % wt.	Demetall degree, % wt.	Residual asphaltenes % wt.	Coke deposits % wt.
1a	(7.0%Co)/Al_2O_3	R	26.0	80.0	2.1	2.8
1b	(7.0%Co)/Al_2O_3	S	19.4	80.0	2.0	3.5
2a	(7.4%Co)/SiO_2	R	55.7	95.6	0.5	2.0
2b	(7.4%Co)/SiO_2	S	13.6	89.0	1.3	3.5
3a	(7.6%Ni)/Al_2O_3	R	18.0	82.0	1.2	5.0
3b	(7.6%Ni)/Al_2O_3	S	30.8	80.0	2.0	6.8
4a	(7.3%Ni)/SiO_2	R	16.5	90.5	1.0	3.0
4b	(7.3%Ni)/SiO_2	S	28.0	78.0	1.8	3.4
5a	(3.4%Co+4.1%Ni)/Al_2O_3	R	21.5	76.0	2.7	3.2
5b	(3.4%Co+4.1%Ni)/Al_2O_3	S	46.0	61.0	3.8	4.6
6a	(3.5%Co+3.5%Ni)/SiO_2	R	27.0	79.0	2.4	2.4
6b	(3.5%Co+3.5%Ni)/SiO_2	S	20.5	76.0	2.6	2.8
7	(Ni+Mo)/Al_2O_3**	S	32.9	75.5	2.8	10.5

*) R - reduction; S - sulfidation after reduction; **) commercial catalyst

A NEW LASER DIAGNOSTIC TECHNIQUE TO EVALUATE CHEMICAL TIME DELAY IN HYPERGOLIC SYSTEMS

Lynette O. Mays, Mark J. Farmer, James E. Smith, Jr.
Department of Chemical and Materials Engineering
Material Science Building, Room 307
University of Alabama in Huntsville
Huntsville, Alabama 35899

INTRODUCTION

Diagnostic techniques that measure ignition delay times (IDT) of hypergolic reactants are normally classified into a few distinct types. Drop tests are techniques that drop one reactant from a set height into a stationary quantity of the second reactant. Mixing tests are techniques that use a method to enhance mixing of the reactant combinations. Impinging jet techniques are tests that use separate fuel and oxidizer injectors to enhance the mixing rate and simulate engine conditions. Also, a few small scale rocket engines have been equipped to measure ignition delay times.

A typical example of a drop test technique was performed by Broatch[4]. A light beam was focused on a photocell a set distance above the organic fuel, which was located in a crucible. The oxidizer, in a stream of droplets of varying size, broke the light beam as it fell into the fuel. A photocell ended the measurement when it sensed the appearance of a flame. The time between these two events defined the ignition delay for the hypergolic reactant combination. A technique used by Gunn[6] was defined as a mixing test by Paushkin[3] in his review of jet fuels. The only significant difference from Broatch's technique described above was that the quantity of fuel and oxidizer used by Gunn was several times as large. Several milliliters of one reactant was decanted into a similar quantity of the other reactant. The photocell used by Gunn to detect the flame, and the one used in Broatch's technique above, did not indicate the strength of the reaction.

In an effort to reduce the mixing time, a device constructed by Pino[7] caused the pressurized injection of oxidizer through 4 ports directed into a stationary quantity of fuel. The combined quantity of fuel and oxidizer used was approximately 4 milliliters for one test. The results of Pino's testing show no indication of the oxidizer to fuel ratio. Without this variable accounted for, the minimum ignition delay for a reactant combination will not likely be found. Ladanyi and Miller[1] placed a small glass ampoule containing approximately one milliliter of organic under the surface of several milliliters of acid. The glass ampoule was crushed by a steel rod to enhance mixing. The initial measurement was the moment of ampoule crushing. The final measurement was made by a photocell sensing the appearance of a flame. Kilpatrick and Baker[5] used a device that forced both fuel and oxidizer together using high pressure gas hydraulics. The reactants were initially located in separate chambers below pistons which forced the propellants together immediately prior to injection into the combustion chamber. The initiation of the timing measurement was through monitoring of piston movement above the fuel and oxidizer. The end of an ignition delay measurement corresponded to an increase of pressure in the test chamber.

Saad and Goldwasser[8] used impinging fuel and oxidizer jets in their technique. They initiated the ignition delay measurement at the moment the valves for fuel and oxidizer were released. Photocell detection of the flame was again used to end the measurement. The resolution of their oscilloscope was 100 milliseconds/division. As ignition delay values are generally less than 100 milliseconds, the resolution of their technique does not provide the accuracy needed for reactions of this speed. In addition to the drop test technique reported earlier, Broatch[4] also used the technique of impinging jets. He used high speed photography to capture pictures of the combined jets and flame. The ignition delay was calculated from the length of the combined jets to the fully developed flame front. The benefits of the photography technique were to capture the strength of the flame as Broatch varied oxidizer to fuel ratio and temperature, and the ability to photograph phenomena such as pre-ignition boiling of the liquid phase. Spengler and Bauer[9] used impinging jets to test the influence of pressure and varying chemical composition on ignition delay measurements. This technique consisted of starting the timing by contacting the fuel and oxidizer, which completed an electrical circuit. The timing measurement was ended by sensing the flame with a photocell located between the two injectors. This technique for impinging jets seemed to be the only true measure of ignition delay among the three discussed.

If the intent of the ignition delay technique is to screen reactant combinations, then the above testers should provide reliable information on relative performance between these combinations. The new laser diagnostic method developed in our laboratories was designed as a research tool to measure relative performance of hypergolic reactant combinations. The technique developed, more than met this expectation. The technique is the first to provide a measure of the chemical

performance of the reactant combinations. This chemical delay time is independent of the mixing technique used.

EXPERIMENTAL

The entire combustion system is designed to study the reaction rates and mechanisms of hypergolic reactants for the ability to propose alternate, enhanced chemistry. The equipment uses a variety of techniques, including visible and near infrared Raman spectroscopic measurements, to meet these objectives. The system, its component make-up, and procedural steps are detailed in recent publications by M. Farmer, L., Mays and J.E. Smith, Jr.[10,12,13].

RESULTS AND DISCUSSION

Figure 2 shows the digital storage oscilloscope traces resulting from a typical drop test for unsymmetrical dimethylhydrazine (UDMH) contacted with red fuming nitric acid (RFNA). The reactants for the test were obtained from Aldrich Company. The UDMH had a purity of 98%. The RFNA had a nitric acid concentration of 90-95%, with the balance being nitrogen tetroxide. The results in this figure are for an oxidizer to fuel ratio of 2. In Figure 2, the upper trace (channel 1) shows the output from photodiode #1, which monitors the surface of the oxidizer droplet. The lower trace (channel 2) shows the output from photodiode #2, which monitors flame emission.

Various reference points have been added to this figure to identify key features resulting from this technique. Point A on channel 1 represents the moment of contact between the fuel and oxidizer. A pinhole/diode geometry restricts he view of the photodiode to a region from the oxidizer surface to approximately 200 μm above the surface. Once the lower surface of the fuel droplet contacts the oxidizer, a region of rapid linear decrease follows. To consistently reference the ignition time delay to a definable point, we extrapolate this linear region to the initial reference level. An identical approach is used at point B to neglect the shape of the trailing edge of the droplet and any wake that it creates on entry. Thus, the region from point A to point B represents the droplet of fuel from initial contact to final entry into the oxidizer. When the fuel droplet completely enters the oxidizer, the laser light can again fully reach photodiode #1 as illustrated by the return of the signal to its initial reference level.

The response of photodiode #1 in the region from point B to C is representative of a still liquid to air interface. This is the region in which droplet mixing is taking place between fuel and oxidizer by a combination of convection and diffusion between the two reactants. In Figure 2 region B-C represents the time period when mass transfer limited kinetics are occurring. In other words, the rate of reaction is limited by mass transfer and mixing limitations. All methods reviewed above suffer from mixing limitations at some point in the process. Kilpatrick and Baker[5], in their study of mixing rates, stated, "If the complete intermixing could be effected in a time very short compared to the (total) ignition delay time, then the measured delay would be the true chemical delay...." Pino made the same observation during attempts to improve mixing with his technique. Following their logic, if the droplet entry and mixing stages, points A-C, could be minimized or eliminated, then region C-D in Figure 2 would represent the true chemical delay.

At point C, the chemical reaction rate increases rapidly, with the reaction producing a gas phase that decreases the signal from photodiode #1. This decrease in signal is due to the density of the vapor phase forming above the liquid surface. This vapor phase was noticed in the work of Ladanyi and Miller[1] using an injector technique with high speed photography. Upon mixing, they noted a thick vapor cloud released by the liquid phase that filled their combustion chamber. Close examination of the photographs was required to locate the appearance of flame within this dense cloud. This vapor phase results from reactive intermediates being released from the liquid phase.

The combination of heat release from the chemical reaction in the liquid phase and the reactivity of the gaseous intermediates causes ignition in the vapor phase, as defined by point D. This analysis is supported in the literature by the work of Saad and Goldwasser[8], Spengler and Bauer[9], Twardy[2], and Habiballah[15]. For example, Saad and Goldwasser[8] found in their work that the liquid phase generated heat 200 times more rapidly than the gas phase at atmospheric pressure. Twardy[2] found that a minimum droplet diameter was required to generate the heat necessary to cause ignition in the reactive vapor phase.

Durgapal and Venugopal[14] performed an ampoule crushing test similar to Ladanyi and Miller[1] to enhance mixing in the RFNA/UDMH combination. For RFNA that had 92% HNO_3 and 8% N_2O_4, they obtained an ignition delay value of 4.7 milliseconds. This value is much smaller than the IDT value, region A-D in Figure 4, of 16.5 milliseconds. If the time for droplet entry is ignored, then the measure would be of mixing time to ignition, i.e., region B-D in Figure 2, or 9.5 milliseconds. This is not surprising though, as no attempt was made to enhance mixing for

the technique presented in this paper. Therefore, Durgapal and Venugopal[14] should have recorded numbers smaller than those of region B-D. However, it one examines region C-D, then a delay of 1.8 milliseconds is measured. This time is a measure from the moment vaporization begins to increase exponentially to ignition. As all hypergolic systems, upon completion of mixing, produce a vapor phase reaction, this period represents a true measure of chemical performance or the chemical delay time.

The importance of the chemical delay time is seen when one compares hydrazine reacted with RFNA (Figure 3) to UDMH reacted with RFNA (Figure 2). Comparing these figures, we see that the ITD for UDMH/RFNA is only 25% faster than hydrazine/RFNA. When one compares the chemical delay time a 75% increase in the reaction rate is measured. This explains why UDMH/RFNA is preferred over hydrazine/RFNA for propulsion systems.

CONCLUSIONS

A new laser diagnostic technique has been developed to quantitatively measure the chemical performance of hypergolic systems. Past techniques and results show that enhanced mixing can reduce ignition delays in an attempt to approximate the chemical delay time. Regardless of technique, the mixing time associated with hypergolic systems can not be eliminated. This drop test technique shows a region after mixing that characterizes the speed of the reaction alone. The beginning of this region, point C, indicates when free radical generation should be observed to obtain information on the chemical mechanisms involved. This new technique requires smaller quantities of reactants than previous methods making it safer and more cost effective.

ACKNOWLEDGEMENTS

This research is funded by the Army Missile Command, grant #DAA H01-91-D R002/D053, and the Army Research Office, grant #DAA 1104-94-G-0265.

REFERENCES

1. D.J. Ladanyi and R.O. Miller, "Two Methods for Measuring Ignition Delay of Self-Igniting Rocket Propellant Combinations," *Jet Propulsion*, Vol. 26, No. 3, pp. 157-63.
2. H. Twardy, "Studies on the Effect of Fuel Injection on the Ignition Process of the Hydrazine-Nitric Acid System," Jet Propulsion Laboratory, DLR FB 68-85.
3. Y.M. Pauskin, The Chemical Composition and Properties for Fuels for Jet Propulsion, Pergamon Press, New York, 1962.
4. J.D. Broatch, "An Apparatus for the Measurement of Ignition Delays of Self-Igniting Fuels," *Fuels*, Vol. 29, 1950, pp. 106-109.
5. M. Kilpatrick and L. Baker, Jr., *Fifth Symposium on Combustion*, pp. 170-196, New York-London 1955.
6. S.V. Gunn, "The Effects of Several Variables Upon the Ignition Lag of Hypergolic Fuels Oxidized by Nitric Acid," *ARS Journal*, Vol. 22, No. 1, pp. 33-38.
7. M.A. Pino, "A Versatile Ignition Delay Tester for Self-Igniting Rocket Propellants," *Jet Propulsion*, Vol. 25, No. 9, pp. 463-466.
8. M.A. Saad and S.R. Goldwasser, "Role of Pressure in Spontaneous Ignition," AIAA Journal, Vol. 7, No. 8, pp. 1574-1581.
9. G. Spengler and J. Bauer, "Ignition Delay of Hypergolic Rocket Propellants," *Technical Translation 16-U.S. Army*, June 1966.
10. M. Farmer, L. Mays, and J.E. Smith Jr., "A Laser Diagnostic Method to Measure Ignition Time Delays of Hypergolic Reactions," AIAA, January 6-9, 1997.
11. Wade, L.G., Organic Chemistry, 2nd edition, Prentice-Hall, Englewood Cliffs, N.J., 1991, pp. 823-886.
12. Farmer, M., Mays, L., and J.E. Smith, Jr., "A Laser Diagnostic Technique to Measure Rapid Acid-Organic Reaction Phenomena," 1997 AIChE Spring Meeting, paper 140e, Houston, TX, February 1997.
13. Farmer, M., Mays, L., and J.E. Smith, Jr., "The Reaction Rates for Hypergolic Propellants Using Chemical Delay Times," submitted to AIAA, Journal of Propulsion and Power, May 1997.
14. Durgapal, U. C., and Venugopal, V. K., "Hypergolic Ignition of Rocket Propellants with Nitric Acid Containing Dissolved Nitrogen Tetroxide," *AIAA Journal*, Vol 12, No. 11, pp. 1611-1612.
15. Habiballah, M., et al., "Experimental Study of Combustion Processes Involved in Hypergolic Propellant Coaxial Injector Operation," *AIAA/SAE/ASME/ASEE 28th Joint Propulsion Conference and Exhibit*, AIAA-92-3388, July 6-8, 1992.

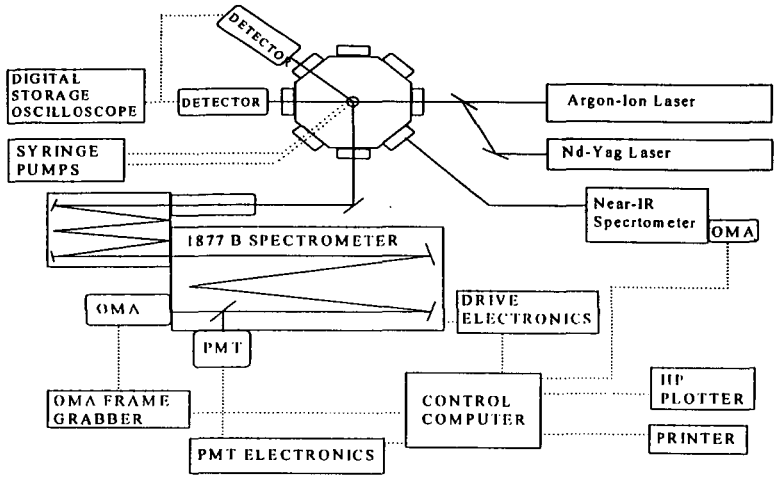

Figure 1. Schematic of the Entire System for Ignition Time Delay and Spectroscopic Analysis

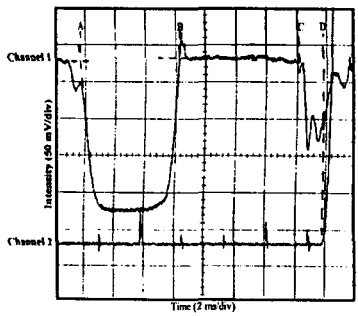

Figure 2. Test Results for UDMH/RFNA

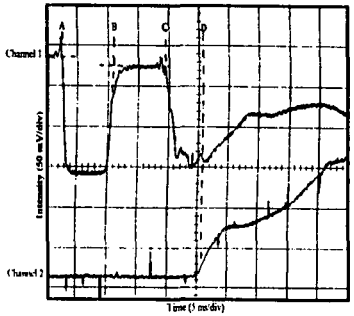

Figure 3. Test Results for Hydrazine/RFNA

USING STRUCTURAL MODELS TO SIMULATE THE POLY-CYCLICS IN COALS.

David L.Wertz
Department of Chemistry and Biochemistry
University of Southern Mississippi
Hattiesburg, MS 39406 USA

Keywords: Poly-cyclic aromatic compounds, molecular modeling, x-ray scattering

INTRODUCTION.

Both NMR[1-4] and other types of analysis[5-10] have recently made significant contributions to understanding the composition and the distribution of the poly-cyclic units which are thought to comprise the most important units in coals. This group[10-13] has recently contributed some x-ray scattering studies which have as their goal a better understanding of the poly-cyclic units. X-ray scattering studies are one-dimensional in nature and address distances in the average scattering unit of a condensed phase material.[14] Structural models of some poly-cyclic (PC) moieties thought to be found in coals have been developed in order to better interpret and understand the x-ray scattering data obtained from these coals. Our models are based on the findings of the NMR and other studies noted above. The structural PC models may be utilized in real space to predict distances between bonded C-C atom-pairs and between non-bonded C··C atom-pairs. In addition, the distance array calculated for each PC model may be Fourier transformed into reciprocal space and compared to the experimentally measured x-ray scattering intensity for a coal (or any other scattering unit).

Whether the analysis occurs in reciprocal space or in real space, the accuracy of the structural models is as important as the accuracy of the x-ray scattering experiments to developing an understanding of the average PC unit in the coal.

EXPERIMENTAL

This group has "built" three-dimensional structural models of several of the poly-cyclic (PC) compounds thought to occur in coals. These models incorporate the "best available" crystallographic data concerning the various C-C bond distances and the C··C·C bond angles as well as information about the planarity of each aromatic ring as well as the co-planarity of each entire PC unit. From the bond distance-bond angle-planarity information, an atom-coordinate map for each of the carbon atoms has been constructed. All of the bonded and non-bonded C··C atom-pair distances have been calculated. The distance array calculated for each PC model has been used to construct a simulated structure curve, in real space, by:

$$W_A(r) = 36\ el^2 \times \sum\{n_{JK}/r_{JK}^{0.5}\} \times \exp(-\gamma \times \Delta r_{JK}^2/r_{JK}^{0.5}). \qquad (1)$$

This real space simulation has been adapted from the Kurrita model for diffraction peaks[15] and is consistent with the shapes of the maxima and minima in the atom-pair correlation functions calculated from x-ray scattering measurements of several of the Argonne Premium Coals.[11-13] In eq. 1, 36 el^2 represents the scattering power of one C-C atom-pair, and n_{JK} represents the number of J-K atom-pairs found at the distance r_{JK} in the average short-range scattering unit of the coal, and $\Delta r_{JK} = r - r_{JK}$.

RESULTS AND DISCUSSION.

Analysis in Real Space. The atom-map and the three-dimensional atomic coordinates developed for naphthalene are presented in Table I. The distance/frequency arrays for naphthalene, anthracene, and phenanthrene are presented in Table II. Shown In Figure I are the simulated real-space structure curves calculated for benzene, naphthalene, anthracene, and naphthacene. Each of these models has been developed based on the first approximation that all of the bonded C-C atom-pair distances are 1.39 Å, that each of the C··C··C bond angles is 120° (i.e., $\phi = 2\pi/3 - \pi/2$ in Table II), and $\tau = 0$ (i.e., the PC rings are co-planar). Numerous other combinations of d, ϕ, and τ have been considered. The longest non-bonded C··C distance is marked by * in each $W_A(r)$. Differences in the longest non-bonded C··C distance and other differences) are clear from comparison of these simulated $W_A(r)$'s.

The simulated structure curve calculated from each model may be compared to the atom-pair correlation function (APCF). The APCF is experimentally determined and

provides a measure of the deviation from randomness of the atom-pairs in the scattering material. The APCF, g(r), is limited to describing a one-dimensional description (i.e., atom-pair distances) which characterize the structuring found in the average short-range structural unit of the subject material (i.e., the coal)and may be obtained from measuring the secondary coherent X rays scattered by the coal.

Correlation between the simulated structure curve calculated from each PCA model, $W_A(r)$, and the experimentally-based atom-pair correlation function, g(r), is initiated by calculating the difference function for each model:

$$\varepsilon_A(r) = W_A(r) - g(r). \quad (2)$$

The difference function is then used to calculate the structure correlation factor for each model by:

$$R_A = \Sigma[\varepsilon_A(r)]^2/\Sigma[g(r)]^2. \quad (3)$$

As with three-dimensional crystal structure analyses, the simulated structure considered to be best representation real-space structure results fram the model which minimizes R_A.

Shown in Table III is are the structure correlatian factars calculated for several PC models campared to the APCF obtained fram Pittsburgh # 8 coal, a high volatile bituminous coal. These comparisans show that g(r) correlates best with the W(r)'s calculated for the two C_{14} PC models> The R_A's praduced for anthracene and for phenanthrene are similar.

Inclusian of the alkyl moieties into the structural model improves the correlation between $W_A(r)$ and g(r) for both phenanthrene and for anthracene. Shown in Figure 2 is a comparison of the $W_{AN}(r)$ with the addition of faur alkyl moieties added to the C_{14} unit. This arrangement produces lower R_A's for bath the anthracene and the phenanthrene models, as seen in Table IV.

Correlatians in Reciprocal Space. The simulated structure curve, W(r), may be Fourier transformed to produce the simulated x-ray scattering intensity in reciprocal space by:

$$J(Q) = \{4\pi/Q\} \times \Sigma n_{JK} \times \int r^2 \times \{W_A(r) - \rho o\} \times \sin (Q \times r) \times \Delta r; \quad (4)$$

where ρ_o is the bulk atom density of the coal.

Defining i(Q) as the experimentally determined intensity in reciprocal space, the comparison between I(Q) and J(Q) may also be used to evaluate the validity of the PC model(s) being considered. Shawn in Figure 3 is the J(Q) calculated from the 4 alkyl-onthracene model compared to I(Q). The correlation factor for the comparison in reciprocal space is termed R*, where:

$$R^* = \Sigma\{i(Q) - J(Q)\}^2/\Sigma\{i(Q)\}^2 \quad (5).$$

Using the alkyl substituted anthracene as the PC model, R* = 0.039 when R* is evaluated from Q = 2.00 Å-1 to 15.00 Å-1. If the region < Q = 2.00 Å-1 is included in the calculation, R* increases dramatically to 0.768; indicating that the large peak in i(Q) centered at 1.7 Å-1 is not due to the average PC structure in the coal. Similar results have been obtained when an alkyl substituted phenanthrene model is used to generate J(Q). All other PCA models produce R* values which are much larger than the R*'s measured for the substituted C_{14} PC's.

CONCLUSIONS

Structural models and detailed atom maps are useful in determining the average PC unit in coals because their simulated structure curves may be directly campared to the results of wide angle x-ray scattering experiments used to examine the coals. However, the resulting statistical analysis does not, necessarily, produce unequivocal results.

REFERENCES

1. Solum, M. S., Pugmire, R. J., and Grant, D. M., *Energy Fuel, 1989 (3) 187.*
2. Muntean, J. V. and Stock, L. M., *Energy Fuel, 1991 (5) 768; 1993 (7) 704.*
3. Franz, J. A., Garcia, R., Lineman, J. C., Love, G. D., and Snape, C. E., *Energy Fuel, 1992 (6) 598.*
4. Codeine, K., Mariti, S., and Nomura, M., *Energy Fuel, 1996 (10) 672.*
5. Winans, R. E., *Am. Chem. Soc., Div. fuel Chem., 1994 (39) 27.*
6. Thiyagarajan, P. and Cody, G. D., *Am. Chem. Soc., Div. Fuel Chem.,* 1997 (42) 253.
7. Takanohashi, T., Iina, M., Kumagai, H., Sanada, Y., and Nakamura, K., "Coal Science". J. A. Pajares and J. M. D. Tascon, ed., Elsevier Science, Amsterdam,

TABLE II. ATOM-PAIR DISTANCE/FREQUENCY ARRAY FOR NAPHTHALENE, ANTHRACENE, AND PHENANTHRENE

DISTANCE (d_{JK})	FREQUENCY (n_{JK}) IN		
	NAPHTHALENE	ANTHRACENE	PHENANTHRENE
1.39 Å	11	17	17
2.47 Å	14	22	21
2.78 Å	6	8	10
3.68 Å	6	12	13
4.17 Å	4	8	10
4.82 Å	2	6	8
5.01 Å	2	4	6
5.56 Å		2	2
6.07 Å		4	2
6.37 Å		4	4
6.96 Å			1
7.23 Å		2	
7.36 Å		2	

TABLE III. STRUCTURE CORRELATION FACTORS BETWEEN SEVERAL PCA MODELS AND THE APCF FOR PITTSBURGH # 8 COAL.

Carbons	PC MODEL	R-VALUEA
C10	naphthalene	0.303
C14	anthracene	0.053
	phenanthrene	0.079
C16	pyrene	0.334
C18	naphthacene	0.750
	1,2-benzophenonthrene	0.553
	crysene	0.568
	tri-phenylene	0.396

[A] R has been calculated over the interval from r = 0.00 Å to r = 10.00 Å.

TABLE IV. EFFECTS OF ADDING FOUR ALKYLS TO THE C_{14} PC MODELS.

PC MODEL	4 ALKYS ADDED	R_A
Anthracene	no	0.053
	yes	0.046 to 0.037[A]
Phenanthrene	no	0.079
	yes	0.062 to 0.040[A]

[A] The actual value of the structural correlation factor depends upon the relative positions of the alkyls as added to the C_{14} unit.

1995, 55.
8. Stock, L.M. and Obeng, M., *ibid.*, p. 67.
9. Winans, R. E., Kim. Y., Hunt, J. E., and McBeth, R. L., *ibid.*, 87.
10. Zhan, Q., Zenobi, R., Buseck, P. R, and Teerman, S., *Energy Fuel, 1997* (11) 144.
11. Wertz, D. L.. and Bissell, M., *Adv. X-Ray Anal., 1994* (37) 491.
12. Wertz, D. L. and Bissell, M., *Fuel, 1995* (74) 1431.
13. Wertz, D. L. and Bissell, M, *Energy Fuel,* 1994 (8) 613.
14. Kruh, R. F.., *Chem. Rev.*, 1962 (62) 314.
15. Kurita, M., *Adv. x-Ray Anal., 1987* (31) 277.

TABLE I. ATOM MAP AND ATOM LOCATIONS FOR NAPHTHALENE

A. ATOM MAP.

TOP VIEW OF XY PLANE SIDE VIEW, XZ PLANE

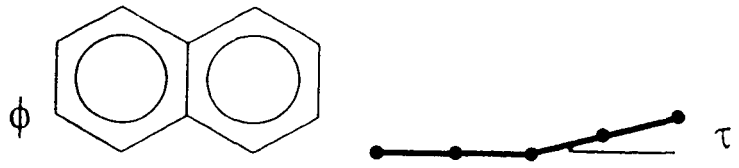

B. ATOM LOCATIONS.

CARBON		ATOM LOCATIONS	
NUMBER	X	Y	Z
1	0	0	0
2	0	d	0
3	d×cosϕ	d×[1+sinϕ]	0
4	2×d×cosϕ	d	0
5	2×d×cosϕ	0	0
6	d×cosϕ	-d×sinϕ	0
7	d×cosϕ×[2+cosτ]	-d×sinϕ	d×cosϕ×sinτ
8	2×d×cosϕ×[1+cosτ]	0	2×d×cosϕ×sinτ
9	2×d×cosϕ×[1+cosτ]	d	2×d×cosϕ×sinτ
10	d×cosϕ×[2+cosτ]	d×[1+sinϕ]	d×cosϕ×sinτ

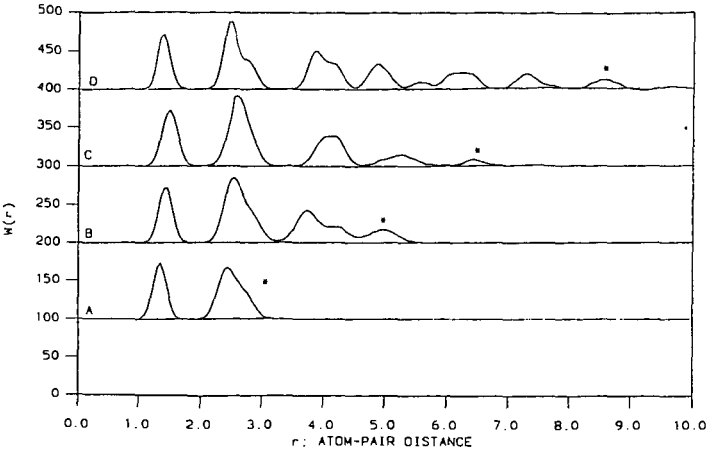

Figure 1. W(r)'s for benzene (A), naphthalene (B), anthracene (C), and naphthacene (D). The longest non-bonded C··C distance in each is marked by *.

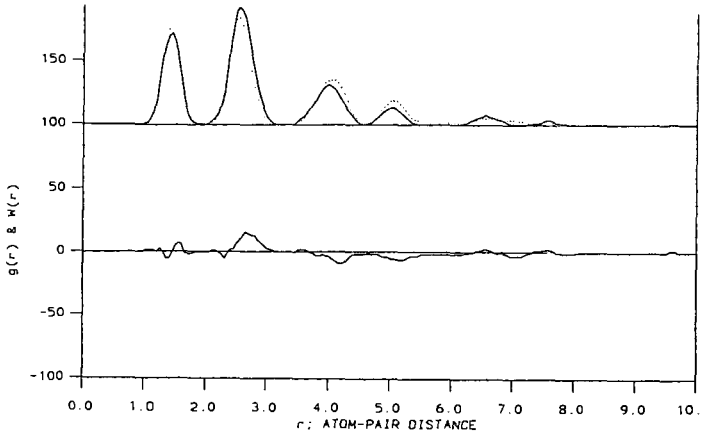

Figure 2. W(r) for the alkylated C_{14} PC {....} compared to the APCF {____}. The ε(r) for this comparison is shown below.

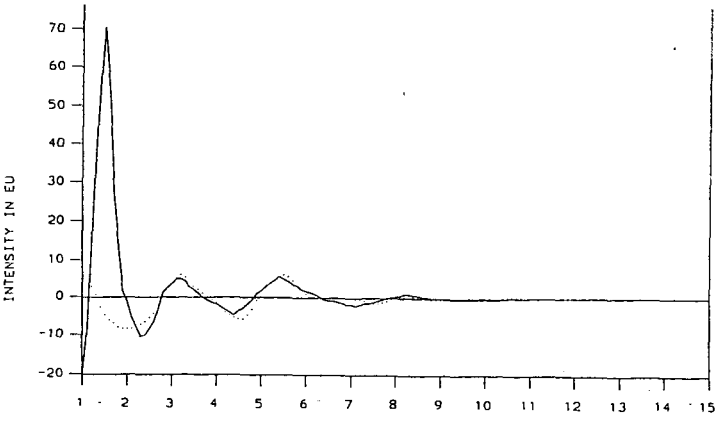

Figure 3. Comparison in reciprocal space of the simulated intensity for an alkylated C_{14} PC unit {....} and the experimentally measured intensity {____}.

EFFECTS OF TEMPERATURE AND PRESSURE ON THE STRUCTURE OF FGD SCRUBBER SLUDGE

S. P. Kelley[1], P. S. Valimbe[1], V. M. Malhotra[1], and D. D. Banerjee[2]
(1) Department of Physics, Southern Illinois University, Carbondale, IL 62901
(2) Illinois Clean Coal Institute, Carterville, IL 62918.

ABSTRACT

Approximately 20 million tons of flue gas desulfurization (FGD) residue are generated in the US every year. To find cost effective disposal approaches for FGD residue, we are attempting to fabricate composite materials from the sludges. We subjected the as- received scrubber sludge (CWLP, Springfield, Illinois) and the sludge which had been dried at 180°C to various formation pressures and temperatures to form 3.2 and 5.7 cm diameter cylinders. The chemical and physical structures of the pressurized materials were probed using scanning electron microscopy (SEM), transmission-Fourier transform infrared (FTIR), and differential scanning calorimetry (DSC) techniques. The formation temperature ($20°C < T < 220°C$) and pressure ($400 \text{ psi} < P < 5500 \text{ psi}$) were variables. The formation pressure did not affect the crystal growth habits of the materials. However, the formation temperature not only controlled the size of the crystallites in our materials, but it also influenced the chemical structure of the fabricated materials.

INTRODUCTION

In the past when electric power utilities shifted from oil to coal for electric power generation, it created environmental concerns related to the emission of SO_x and NO_x from the combustion of coal [1]. These gases are formed in combustion units due to oxidation of sulfur and nitrogen present in coal. To mitigate environmental concerns, various technologies have been developed including Flue Gas Desulfurization (FGD). FGD technology involves the use of scrubbers which utilize lime or limestone to capture the flue gasses. Unfortunately, though FGD technology is successful in reducing the emission of undesirable gases, it generates a large quantity of solid waste in the form of scrubber sludge. In fact, approximately 20 million tons of FGD residues are generated annually in the United States. The properties of these solid wastes strongly depend on the type of coal used in the combustion units as well as the desulfurization process employed [2]. In general, the scrubber sludge is believed to contain mostly gypsum ($CaSO_4.2H_2O$), calcium sulfate ($CaSO_4$), calcium sulfite ($CaSO_3$), calcite ($CaCO_3$), and in addition small quantities of fly ash and excess reagents [3,4]. Of the different types, wet scrubber units are the most commonly used for SO_2 removal from flue gases. The purity of gypsum obtained from a wet scrubber unit is believed to range from 95% to 99%.

The disposal of 20 million tons of scrubber sludge annually is in itself becoming a serious economic problem for coal utilities. Even though different usages of scrubber sludges have been proposed in road base construction [5,6], prefabricated products (gypsum boards) [7], the cement industry [5,7], plaster fabrication [7], and agriculture [7,8], their overall utilization is still very small. This is largely due to the changes in the sludges' properties from batch to batch and unit to unit as well as to market specifications and seasonal variations. Unfortunately, a major portion of the total amount of scrubber sludge generated continues to be dumped in landfills.

The implementation of the Clean Air Act of 1990 will require new utilization of scrubber sludges. Proposed applications of synthetic gypsum, produced by certain power plants, are the formation of plaster [7], formation of binder material, self leveling floor screeds, and fiber reinforced slabs from FGD sludge [9]. In addition, we have been exploring techniques of forming structural composite materials from both sulfate- and sulfite-rich FGD sludges. Before these technologies can be matured, we must understand how formation pressure and temperature affect the crystalline growth habits of the sludge and how these parameters affect the structure of the formed material. Therefore, we subjected a sulfate-rich scrubber sludge to various structural formation conditions and examined the formed materials with the help of SEM, DSC, and FTIR techniques.

EXPERIMENTAL TECHNIQUES

The present study is based on materials fabricated from a scrubber sludge generated by the City Water and Light Power plant (CWLP) in Springfield, Illinois. The scrubber sludge sample was obtained from the sample bank maintained by the Department of Mining Engineering at Southern Illinois University, Carbondale, Illinois. The as-received sample was in a thick slurry form, and

the sample was air dried at room temperature prior to fabricating materials from it. Our characterization studies showed this material to be largely $CaSO_4.2H_2O$ [10].

The cylindrical disks of the material were formed by hot pressing the CWLP scrubber sludge in dies of diameter 3.2 cm and 5.7 cm, respectively. The length of the cylinders varied from 2.5 cm to 7.5 cm. We used temperature ($20°C < T < 220°C$), pressure ($400 \text{ psi} < P < 5000 \text{ psi}$), and hot pressing time ($15 \text{ min.} < T < 120 \text{ min.}$) as variables in forming the materials. We fabricated our disks using two different methods. In the first, the air dried samples were used with water to form a slurry paste, which was subjected to the conditions mentioned above. In the second approach, the CWLP scrubber sludge was thermally treated in air at 180°C for two hours to convert the sludge into hemihydrate ($CaSO_4.0.5H_2O$) crystals. This white powdery material was then combined with water to form a slurry [11] which was subsequently used to form the cylinders as described above. The formation parameter summary and identification of the samples are listed in Table 1.

Table 1
The sample identity and formation conditions of cylindrical disks.

Sample Identity	Formation Conditions		
	Time (minutes)	Pressure (psi)	Temperature (°C)
CWLP A1	20	5,000	24
CWLP A2	20	4,000	24
CWLP A3	20	3,000	24
CWLP A4	20	2,000	24
CWLP B1	20	4,000	60
CWLP B2	20	4,000	100
CWLP B3	20	4,000	140
CWLP B4	20	4,000	180
SPK 31	90	2,500	94
SPK 32	90	2,500	125
SPK 29	90	2,500	200
SPK 33	90	500	160
SPK 34	90	1,500	160
SPK 35	90	4,500	160

The morphology of the crystallites formed in our cylinders was studied using a Hitachi S570 scanning electron microscope. Initially, we cut small pieces of the cylinder with the help of a diamond saw. However, our SEM results exhibited smooth surface textures of the cut material, clearly indicating that the sawing itself affected the crystallites. Therefore, the samples were prepared by breaking the cylinders and extracting small pieces of the material from the interior as well as from the exterior of the cylinders. The pieces were mounted on the SEM sample stubs, using carbon paint, and were placed in an oven at 60°C for 24 hours to allow their fixation on the stubs. The samples, thus mounted, were sputter coated with a 40 nm of Ag/Pd layer to avoid the problem of charging. The SEM study was carried out using an accelerating voltage of 20 kV.

The thermal behavior of the fabricated materials, i.e., CWLP Ax (x = 1,2,3 or 4), CWLP Bx (x = 1, 2, 3, or 4), and SPKxx (xx = 29, 31, 32, 33, 34, or 35) was recorded using a Perkin-Elmer DSC7 system [12, 13]. To record the DSC thermographs at $40°C < T < 300°C$, the samples were sealed in aluminum pans with a hole drilled in them so that gases or vapors could escape easily. The transmission-FTIR data were collected using a nujol mull technique. Thin films of nujol mull, containing the ground sample, were formed on the KBr windows. The FTIR spectra of the various samples were recorded at 4 cm^{-1} resolution using an IBM IR44 FTIR spectrometer.

RESULTS AND DISCUSSION

Microscopic Results: The CWLP Ax series was formed with a view to explore how pressure affects the crystal growth habit of sludge-derived hemihydrate powder at room temperature.

Figure 1 reproduces the microphotograph of CWLP A1 sample. The SEM pictures revealed that for all CWLP Ax series the crystals were mostly needle-shaped with thin needles ranging from 2.5 μm to 40 μm in length. However, most of the crystals were around 2.5 μm in length. On average the thickness of the needles was about 2.5 μm. A similar compact, needle-shaped crystal growth habit has been reported for hydrated calcium sulfate when hemihydrate crystals were exposed to water vapor [14]. We did not observe any effect of pressure on the growth habit of crystallites for CWLP Ax series.

The effect of temperature on the crystallization behavior of hemihydrate was studied by fabricating CWLP Bx series in which a hemihydrate-water slurry was hot pressed at 50°C < T < 200°C at a constant pressure of 4000 psi. Similar to the results of CWLP Ax series, CWLP B1 sample also showed small needle-shaped crystals of gypsum. This sample was fabricated at 60°C. As the fabrication temperature increased, the size of crystallites formed in the sample also increased. This can be clearly seen in Fig. 2 which depicts the SEM photograph of CWLP B4 sample grown at 180°C. SEM pictures of CWLP B2 fabricated at 100°C showed a few small parallelogram-shaped crystals (length ~ 18 μm, thickness ~ 3 μm) in addition to mostly needle-shaped crystals. The parallelogram-shaped crystals are a typical morphology for gypsum [10]. On increasing the formation temperature to 140°C and 180°C, we observed not only the increase in the size of crystals formed but interestingly also the cession of needle-shaped crystals. Large interlocked crystals over the range from 20 μm to 240 μm in length and of thicknesses varying from 5 μm to 50 μm were formed at 180°C. It appears from our results that while formation pressure has only a marginal effect on the crystal growth habit, the formation temperature drastically alters the crystal growth behavior of sludge-derived hemihydrate.

In the second set of experiments, we examined how pressure and temperature affected the crystal growth habits of as-received scrubber sludge, i.e., gypsum-water slurry. Unlike previously discussed results, where we converted the sludge into hemihydrate powder by heating the sludge at 180°C (CWLP Ax and CWLP Bx series), in the present set of experiments (SPKxx series) the sludge was only air dried at room temperature prior to forming the materials. Figure 3 shows SEM microphotograph of SPK31 sample, which clearly shows large crystals are formed ranging from 6 μm to 50 μm in length, while the thickness varied from 2 μm to 20 μm. A comparison of these dimensions with those of CWLP B2 led us to conclude that the starting phase of the hydrated calcium sulfate influences the size and morphology of the crystals formed at T < 140°C. On increasing the formation temperature to 125°C (SPK32 sample), a further increase in the dimensions of the crystals resulted. For SPK31 particle size ranged from 8 μm to more than 100 μm in lengths and thickness varied from 8 μm to 30 μm. However, an increase in temperature to 200°C revealed that crystals started to form which resembled needle-like shapes and the crystallites were compacted in the sample.

The SPK33, SPK34, and SPK35 samples were formed at a fixed temperature of 160°C using different pressures. A comparative analysis of SEM pictures of SPK33 and SPK 35 showed that while the surfaces of the crystallites in SPK35 (formed at 4500 psi) had considerable roughness and flaky-like appearance, this was not the case for SPK33 which was formed at a much lower pressure, i.e., 500 psi. Since both samples were fabricated by hot pressing the slurry at the same temperature for equal lengths of time, it was possible that the surface roughness observed for SPK35 sample was the consequence of higher pressure used. One possible explanation could be that these flaky structures were formed by escaping water molecules, thus leaving traces of "water channels". These traces were oriented in one particular direction, i.e., in the longitudinal direction of the crystallites. Since under our hot pressing conditions, the water vapors could only escape from the rim of our die, therefore, it was not surprising to observe oriented defects on the surface of the crystallites. The crystal dimensions were not affected by the pressure applied like for CWLP Ax series, and in general crystallite sizes varied from 10 μm to 90 μm in length and 4 μm to 30 μm in thickness.

Thermal and Infrared Results: It is well known [10,15,16] that gypsum undergoes a two step dehydration process at 110°C < T < 220°C. Therefore, DSC experiments could be used to identify the phases of the calcium sulfate formed in our materials. For example, Fig. 4 reproduces the observed DSC thermographs of SPK29 and SPK31 samples formed at 2500 psi pressure at 94°C and 200°C, respectively. Two endothermic peaks were observed for SPK31 sample at around 170°C and 195°C, while a single endothermic peak was seen for SPK29 sample at around 195°C. In our thermal characterization measurements on CWLP scrubber sludge [10], we observed two endothermic peaks centered at around 154°C and 189°C. The first endothermic peak was associated with $CaSO_4.2H_2O$ decomposing into $CaSO_4.0.5H_2O$ and the second endothermic peak with the dehydration of $CaSO_4.0.5H_2O$ into $CaSO_4$. The shift in the peak temperatures seen for SPK31 sample could be attributed to the compaction of the crystallites,

presenting additional mechanical barriers for water's desorption. Thus, shifts in the temperatures of endothermic peaks were produced. It is therefore argued that while SPK31 sample crystallized perhaps in gypsum phase, the crystallites formed in SPK29 sample were hemihydrate. All the samples fabricated in CWLP Ax and CWLP Bx series exhibited a two-step dehydration endothermic reaction. This result leads us to believe that the gypsum crystallites were present in all these fabricated samples. Whether hemihydrate phase was also present can not be answered from DSC measurements alone since the presence of both gypsum and hemihydrate phases in the sample will still generate two endothermic reactions. However, it is possible for us to argue that only hemihydrate phase was formed for SPK29, SPK33, SPK34, and SPK35 samples since we observed a single endothermic reaction at around 190°C.

Infrared spectroscopic technique [10,17] can be used to further verify and identify which calcium sulfate phases have formed in our fabricated cylinders. In water's stretching region, gypsum produces three vibrational modes at around 3550, 3490 (weak band), and 3400 cm^{-1}; while in the bending region, two distinct oscillators are observed at 1686 and 1623 cm^{-1}. For hemihydrate structure, two vibrational bands in the stretching region appear at around 3610 and 3555 cm^{-1}. A single vibrational mode is seen at around 1620 cm^{-1} for the hemihydrate in the bending region. If anhydrous calcium sulfate phase is present, then that phase will produce no water bands but still can be recognized from SO_4^{2-} ions' vibrations. We have summarized our FTIR results for CWLP Ax, CWLP Bx, and SPKxx series in Table 2. The identified phases are also listed in that table. The CWLP Ax and CWLP Bx (x = 1,2) cylinders were largely composed of gypsum crystallites with some hemihydrate crystallites also present. The CWLP Bx (x = 3, 4) cylinders on the other hand were formed from largely hemihydrate crystallites with some gypsum phase also present in them. It is interesting to note that if as-received, but air dried, CWLP scrubber sludge was used to fabricate the materials then the cylinders, depending upon formation temperature, either crystallized in gypsum or hemihydrate phase rather than in mixed phases like CWLP Ax and CWLP Bx series.

ACKNOWLEDGMENTS

This work was supported in part by Illinois Clean Coal Institute (Illinois Department of Commerce and Community Affairs).

REFERENCES:

1. Randolph, A. D.; Kelly, B. J.; Keough, B. "Calcium Sulfite and Calcium Sulfate Crystallization, Vol.1: Effect of Crystallization Type on Gypsum Size Distribution", *EPRI, Palo Alto, California, Research Project* 1031-3, Nov. 1986.
2. Puri, V.K.; Paul, B. C.; Mukherjee, J.; Hock, K. K.; Yu, Z. "Utilization Coal Refuse and FBC Fly Ash: Strength Aspects", *Procd. NMLRC Sympos, (Eds.) Y. P. Chugh and D. C. Davin*, pp 187-195, 1993.
3. Clarke, L. B. "Management of FGD residues: An International Overview", *Procd. 10th Pittsburgh Coal Conf., (Ed.) S-H Chiang*, pp. 561-566 , 1993.
4. Taulbee, D. N.; Graham, U.; Rathbone, R. F.; Robl, T. L. *Am. Chem. Soc. Prep., Div. Fuel Chem. 40(4), 858, 1995.*
5. Valimbe, P. S.; Malhotra, V. M.; Banerjee, D. D.; *Am. Chem. Soc. Prep., Div. Fuel Chem.*, **40(4)**, 776, 1995.
6. Goodrich-Mahoney, J. W. "Coal Combustion By-products Field Research Program at EPRI: An Overview", *EPRI (Environmental Division)*, 1994.
7. Luckevich, L. M. "Making and Marketing Flue Gas Desulfurization Gypsum", *Procd. 12th Inter. Sympos. on Coal Combustion By-Products Management and Use, Orlando, Florida*, **Vol. 2**, pp 67-1 to 67-7, 1997.
8. Chou, M.-I. M.; Bruinius, J. A.; Li, Y. C.; Rostam-Abadi, M.; Lytle, J. M. *Am. Chem. Soc. Prep., Div. Fuel Chem. 40(4), 896, 1995.*
9. Sclieper, H.; Duda, A.; Jager, R.; Kanig, M.; Kwasny-Echterhagen, R. "FGD Gypsum - A Raw Material for New Binder Systems" *Procd. 12th Inter. Sympos. on Coal Combustion By-Products Management and Use, Orlando, Florida*, **Vol. 2**, pp 48-1 to 48-13, 1997.
10. Valimbe, P. S.; Malhotra, V. M.; Banerjee, D. D.; *Am. Chem. Soc. Prep., Div. Fuel Chem.*, 1997 (this volume).
11. Lynch, W. M. *Am. Ceramic Soc. Bull.* **74**, 60, 1995.
12. Jasty, S.; Malhotra, V. M. *Phys. Rev. B* **45**, 1, 1992.
13. Jasty, S.; Malhotra, V. M.; Robinson, P. D. *J. Physics: Condens. Matter* **4**, 4769, 1992.
14. Gans, W.; Klocker, H.; Knacke, O. Z. Metallkd. **87**, 98, 1996.
15. Blaine, R. *American Laboratory*, **Sept. 1995**, pp 24-28.

16. Dunn, J. G.; Oliver, K.; Sills, I. *Thermochim. Acta* **155**, 93, 1989.
17. Bensted, J.; Prakash, S. *Nature* **219**, 60, 1968.

Table 2
The observed water bands for various samples fabricated from CWLP scrubber sludge and the possible crystallite phases. CWLP HP represents hemihydrate phase derived from the sludge by heating it at ambient pressure at 180°C.

Sample Name	Water Stretching Vibrations (cm^{-1})	Water Bending Band (cm^{-1})	Phase Identified
CWLP HP	3607, 3553, 3406	1622	Largely Hemihydrate
CWLP A4	3607, 3551, 3404	1685, 1622	Gypsum + Hemihydrate
CWLP A1	3608, 3553, 3404	1685, 1622	Gypsum + Hemihydrate
CWLP B1	3607, 3545, 3400	1686, 1620	Gypsum + Hemihydrate
CWLP B2	3607, 3553, 3404	1686, 1620	Gypsum + Hemihydrate
CWLP B3	3609, 3553, 3404	1685, 1620	Hemihydrate + Gypsum
CWLP B4	3607, 3553, 3404	1685, 1620	Hemihydrate + Gypsum
SPK 31	3543, 3493, 3400	1688, 1622	Gypsum
SPK 32	3545, 3493, 3400	1685, 1622	Gypsum
SPK 29	3609, 3555	1618	Hemihydrate
SPK 33	3611, 3555	1621	Hemihydrate
SPK 35	3611, 3555	1620	Hemihydrate

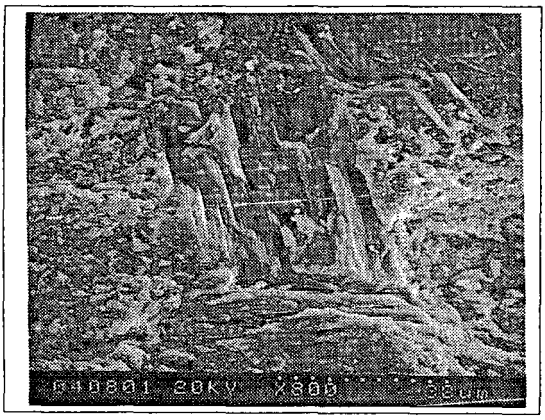

Figure 1. SEM microphotograph of sample fabricated from hemihydrate powder derived from CWLP scrubber sludge. The water slurry was pressed at 5000 psi pressure for 20 minutes at 24°C.

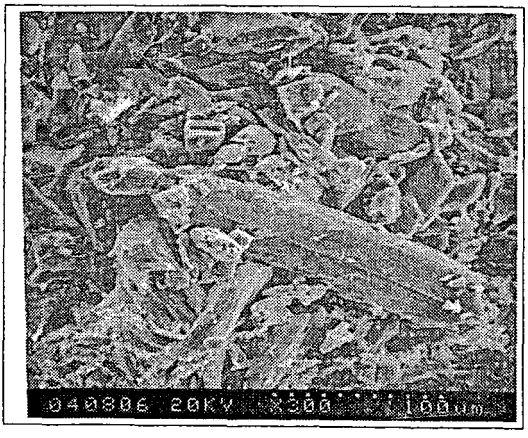

Figure 2. SEM microphotograph of sample fabricated from hemihydrate powder derived from CWLP scrubber sludge. The water slurry was pressed at 4000 psi pressure for 20 minutes at 180°C.

Figure 3. SEM microphotograph of sample fabricated from CWLP scrubber sludge. The water slurry was pressed at 2500 psi pressure for 90 minutes at 94°C.

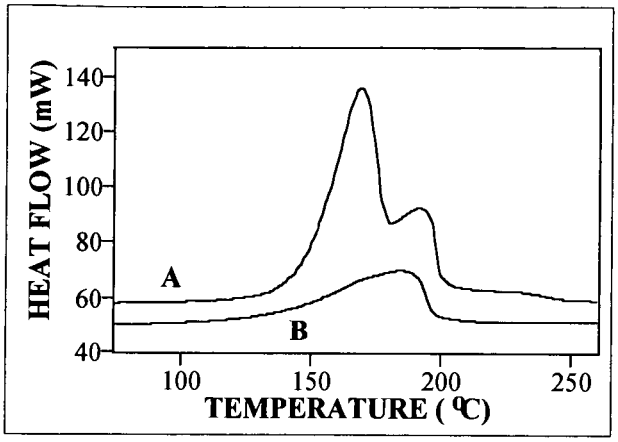

Figure 4. The observed DSC thermographs for (A) SPK31 sample formed at 94°C at 2500 psi pressure and (B) SPK29 sample fabricated at 200°C at 2500 psi pressure.